










# eIF3 mRNA selectivity profiling reveals eIF3k as a cancer-relevant regulator of ribosome content

Haoran Duan<sup>1,†</sup> , Siqiong Zhang<sup>1</sup>, Yoram Zarai<sup>2</sup>, Rupert Öllinger<sup>3</sup> , Yanmeng Wu<sup>1</sup>, Li Sun<sup>1</sup>, Cheng Hu<sup>1</sup>, Yaohui He<sup>1</sup>, Guiyou Tian<sup>1,‡</sup> , Roland Rad<sup>3,4,5</sup> , Xiangquan Kong<sup>6,\*</sup> , Yabin Cheng<sup>1,\*\*</sup> , Tamir Tuller<sup>2,7</sup> & Dieter A Wolf<sup>1,5,\*\*\*,†</sup> 

## Abstract

eIF3, whose subunits are frequently overexpressed in cancer, regulates mRNA translation from initiation to termination, but mRNA-selective functions of individual subunits remain poorly defined. Using multiomic profiling upon acute depletion of eIF3 subunits, we observed that while eIF3a, b, e, and f markedly differed in their impact on eIF3 holo-complex formation and translation, they were each required for cancer cell proliferation and tumor growth. Remarkably, eIF3k showed the opposite pattern with depletion promoting global translation, cell proliferation, tumor growth, and stress resistance through repressing the synthesis of ribosomal proteins, especially RPS15A. Whereas ectopic expression of RPS15A mimicked the anabolic effects of eIF3k depletion, disruption of eIF3 binding to the 5'-UTR of *RPS15A* mRNA negated them. eIF3k and eIF3l are selectively downregulated in response to endoplasmic reticulum and oxidative stress. Supported by mathematical modeling, our data uncover eIF3k-l as a mRNA-specific module which, through controlling *RPS15A* translation, serves as a rheostat of ribosome content, possibly to secure spare translational capacity that can be mobilized during stress.

**Keywords** cancer growth control; mRNA selectivity; ribosome content; RPS15A; translation initiation factor 3

**Subject Category** Translation & Protein Quality

**DOI** 10.15252/emboj.2022112362 | Received 16 August 2022 | Revised 4 March 2023 | Accepted 20 April 2023 | Published online 8 May 2023

**The EMBO Journal (2023) 42: e112362**

## Introduction

Protein synthesis is a complex process requiring tight coordination of discrete steps including the initiation of mRNA translation, translation elongation and termination as well as co-translational folding, subcellular targeting, and quality control of the nascent polypeptides. In canonical initiation, mRNA is recruited to the ribosome through eIF4E-mediated binding of the m7G cap. eIF4E together with eIF4G then recruits to the mRNA a complex consisting of eIF3 and the 40S ribosome loaded with methionyl-tRNA and additional eIFs (Sonenberg & Hinnebusch, 2009). Upon scanning for the start codon, the 60S ribosomal subunit joins to produce an actively translating 80S ribosome.

Apart from canonical translation initiation via the 5'-cap, the 13-subunit eIF3 complex mediates several noncanonical modes of initiation through direct interaction with mRNAs or mRNA-binding proteins (Wolf *et al.*, 2020). Using PAR-CLIP, eIF3 was shown to interact with structured 5'-UTR motifs of hundreds of mRNAs, resulting in translational activation or repression (Lee *et al.*, 2015). For example, phosphorylation-controlled binding of eIF3 to c-Jun mRNA was shown to regulate its cap-dependent but eIF4E-independent function in translation (Lee *et al.*, 2016; Lamper *et al.*, 2020). Likewise, transient recruitment of eIF3 to their 3'-UTRs promotes a burst in the translation of mRNAs encoding T cell receptors (De Silva *et al.*, 2021). Conversely, binding of eIF3 to the ferritin light chain mRNA led to the inhibition of its translation (Pulos-Holmes *et al.*, 2019). In addition, eIF3-binding sites in mRNAs frequently overlap with sites of N6 methyl adenosine (m6A) modification, and eIF3 was shown to bind to m6A either directly or through m6A reader and writer proteins (Meyer *et al.*, 2015; Wolf *et al.*, 2020). Thus, eIF3 is positively as well as

1 State Key Laboratory of Stress Biology and Fujian Provincial Key Laboratory of Innovative Drug Target Research, School of Pharmaceutical Sciences, Xiamen University, Xiamen, China

2 Department of Biomedical Engineering, Tel Aviv University, Tel Aviv, Israel

3 Institute of Molecular Oncology and Functional Genomics and Center for Translational Cancer Research (TranslaTUM), School of Medicine, Technical University of Munich, Munich, Germany

4 German Cancer Consortium (DKTK), German Cancer Research Center (DKFZ), Heidelberg, Germany

5 Department of Internal Medicine II, Klinikum rechts der Isar, Technical University Munich, Munich, Germany

6 Department of Radiation Oncology, Xiamen Humanity Hospital, Fujian Medical University, Xiamen, China

7 The Sagol School of Neuroscience, Tel-Aviv University, Tel Aviv, Israel

\*Corresponding author. Tel: +86 138 0508 9583; E-mail: kongxiangquan2020@aliyun.com

\*\*Corresponding author. Tel: +86 182 5071 0937; E-mail: chengyb@xmu.edu.cn

\*\*\*Corresponding author. Tel: +86 151 6841 0404; E-mail: dawolf@westlake.edu.cn

†Present address: Westlake Laboratory of Life Sciences and Biomedicine and School of Life Sciences, Westlake University, Hangzhou, China

‡Present address: Ganzhou Key Laboratory for Drug Screening and Discovery, School of Geography and Environmental Engineering, Gannan Normal University, Ganzhou, China

negatively involved in many different forms of canonical and non-canonical translation initiation.

However, not all eIF3 subunits are essential for protein synthesis, cell growth, and survival (Wagner *et al*, 2016), suggesting that some have mRNA-selective functions that underlie eIF3's multifunctionality. For example, we have reported that subunits eIF3d and eIF3e constitute a module within the eIF3 holo-complex that selectively promotes the synthesis of proteins with membrane-associated functions, including subunits of the mitochondrial electron transport chain (ETC; Shah *et al*, 2016; Lin *et al*, 2020). Likewise, eIF3f was shown to advance sperm-specific translation through interaction with proteins that bind MIWI/piRNAs in 3'-UTRs, thus leading to circularization of mRNA which is thought to promote translation (Dai *et al*, 2019). Even more recently, eIF3g was implicated in neuron-specific translation in *Caenorhabditis elegans* (Blazie *et al*, 2021). Furthermore, eIF3c was shown to be dispensable for global translation and viability in mice but to direct the translation of the Sonic Hedgehog receptor PTCH1 through a pyrimidine-rich motif in the 5'-UTR (Fujii *et al*, 2021). Finally, the eIF3k-l module was reported to be dispensable for viability in *C. elegans*, whereas its removal enhances stress resistance, although this effect remains to be attributed to mRNA-selective changes in translation (Cattie *et al*, 2016). To date, no study has assessed the impact on holo-complex formation and mRNA-specific translation of individually disabling multiple eIF3 subunits in the same system.

In terms of human physiology, many eIF3 subunits are overexpressed in cancer and can drive *de novo* holo-complex formation and increased protein synthesis along with cell transformation *in vitro* (Hershey, 2015). However, despite striking progress in the structural analysis of the eIF3 complex (Hashem *et al*, 2013; des Georges *et al*, 2015; Simonetti *et al*, 2016; Eliseev *et al*, 2018; Thoms *et al*, 2020), mechanistic insight into the mRNA-selective functions of eIF3 subunits remains scarce and no drugs exist to target eIF3 in cancer or other diseases.

Assembly and dissociation of the eIF3 complex is known to proceed in an ordered fashion according to structural modules (Zhou *et al*, 2008; Wagner *et al*, 2014, 2016; Smith *et al*, 2016). Testing the concept that structural modules carry distinct functions, we have embarked on a systematic loss-of-function study to evaluate mRNA selectivity of module-defining eIF3 subunits in cell proliferation and cancer growth. While eIF3a, b, e, and f are found to promote cell proliferation and tumor growth despite regulating distinct sets of mRNAs, eIF3k limits cell and tumor growth by repressing global translation. Mechanistically, this eIF3k-dependent repression is mediated by binding of eIF3k to the 5'-UTR of the mRNA encoding ribosomal protein RPS15A. Our studies define eIF3 as a multifunctional complex consisting of distinct modules imposing positive as well as negative regulation on mRNA-selective translation with the eIF3k-l module serving as a rheostat of ribosome content.

## Results

### Differential requirement of eIF3 subunits for eIF3 holo-complex formation

To assess subunit-specific functions of eIF3, we generated HCT116 colon cancer cell lines in which individual eIF3 subunits can be

rapidly and reversibly depleted by small molecule-induced degradation. We targeted the following eIF3 subunits (Fig 1A): (i) eIF3a, a core subunit known to nucleate the assembly of the holo-complex (Wagner *et al*, 2016; Smith *et al*, 2016, 3), (ii) eIF3b, a subunit of the distinct "b-g-i" module, (iii) eIF3f, a subunit which was reported to inhibit rather than activate translation (Shi *et al*, 2006; Aguero *et al*, 2017), (iv) eIF3e, a subunit of the "d-e" module involved in the synthesis of membrane-associated proteins (Shah *et al*, 2016; Lin *et al*, 2020), and (v) eIF3k, a subunit of the nonessential "k-l" module, which has cryptic mRNA cap-binding activity through eIF3l (Kumar *et al*, 2016). We used CRISPR-mediated genome editing to add the auxin-inducible degradation domain (mAID) to both alleles of eIF3a, b, e, f, and k (Natsume *et al*, 2016). In addition, both alleles of each gene were modified with either mClover or mCherry for allele-specific protein imaging (Fig EV1A). Fluorescence microscopy revealed predominantly cytoplasmic localization of all five eIF3 subunits (Fig EV1B), a pattern which is consistent with their established role in cytoplasmic mRNA translation. Thus, epitope tagging with mAID and fluorescent proteins does not seem to interfere with normal subcellular localization of eIF3 subunits.

Unlike RNAi-mediated depletion of eIF3 subunits for prolonged duration (e.g., 3 days; Wagner *et al*, 2016) and potentially marked by variable efficiency and off-target activity, auxin-induced degradation led to acute depletion, thus minimizing adaptive effects expected after long-term depletion. For example, eIF3b-mAID was selectively downregulated within 2 h of auxin (IAA) addition, whereas the expression of the remaining seven eIF3 subunits tested was not majorly affected (Fig EV1C). eIF3a-mAID and eIF3f-mAID not only showed a similar depletion but also led to co-depletion of eIF3k (Fig EV1C). Depletion of eIF3e-mAID caused co-depletion of eIF3d and eIF3k as observed previously (Yen & Chang, 2000; Shah *et al*, 2016; Wagner *et al*, 2016), while depletion of eIF3k co-depleted eIF3l (Fig 1B, Appendix Fig S1) as reported (Wagner *et al*, 2016). Addition of IAA to parental HCT116 cells had no effect on the expression of eIF3 subunits.

We next determined the consequences of depleting eIF3 subunits for eIF3 holo-complex formation by quantitative SILAC proteomics (Cox *et al*, 2009). For this, we maintained eIF3-mAID cell lines either in regular "light" (L) media or in media supplemented with stable "heavy" (H) lysine and arginine. Heavy-labeled cells were treated with IAA for 12 h to shut off the expression of eIF3 subunits. eIF3 was immunopurified from both conditions using antibodies against eIF3b or eIF3c. Upon trypsin digestion, corresponding L (DMSO control) and H (IAA) samples were mixed and analyzed by LC-MS/MS to obtain the ratios of eIF3 subunits engaged in eIF3 complexes before and after depletion of individual subunits. The H/L ratios of eIF3 subunits were normalized to the bait, either eIF3b or eIF3c, depending on which antibody was used for purification, and plotted as a heatmap (Fig 1C).

The data showed that acute depletion of eIF3a led to the disassembly of ~ 60% of holo-eIF3 while largely sparing the eIF3b-g-i subcomplex (Figs 1C and D, and EV2A). Conversely, depletion of eIF3b led to a ~ 60% depletion of the eIF3b-g-i subcomplex, while mostly maintaining the octameric core complex. Depletion of eIF3e affected holo-eIF3 formation similarly to depletion of eIF3f, leading to a ~ 80% depletion but leaving largely intact a residual complex consisting of eIF3a, b, g, i, and j, which closely resembles the essential core complex present in *S. cerevisiae* (Valášek *et al*, 2017).

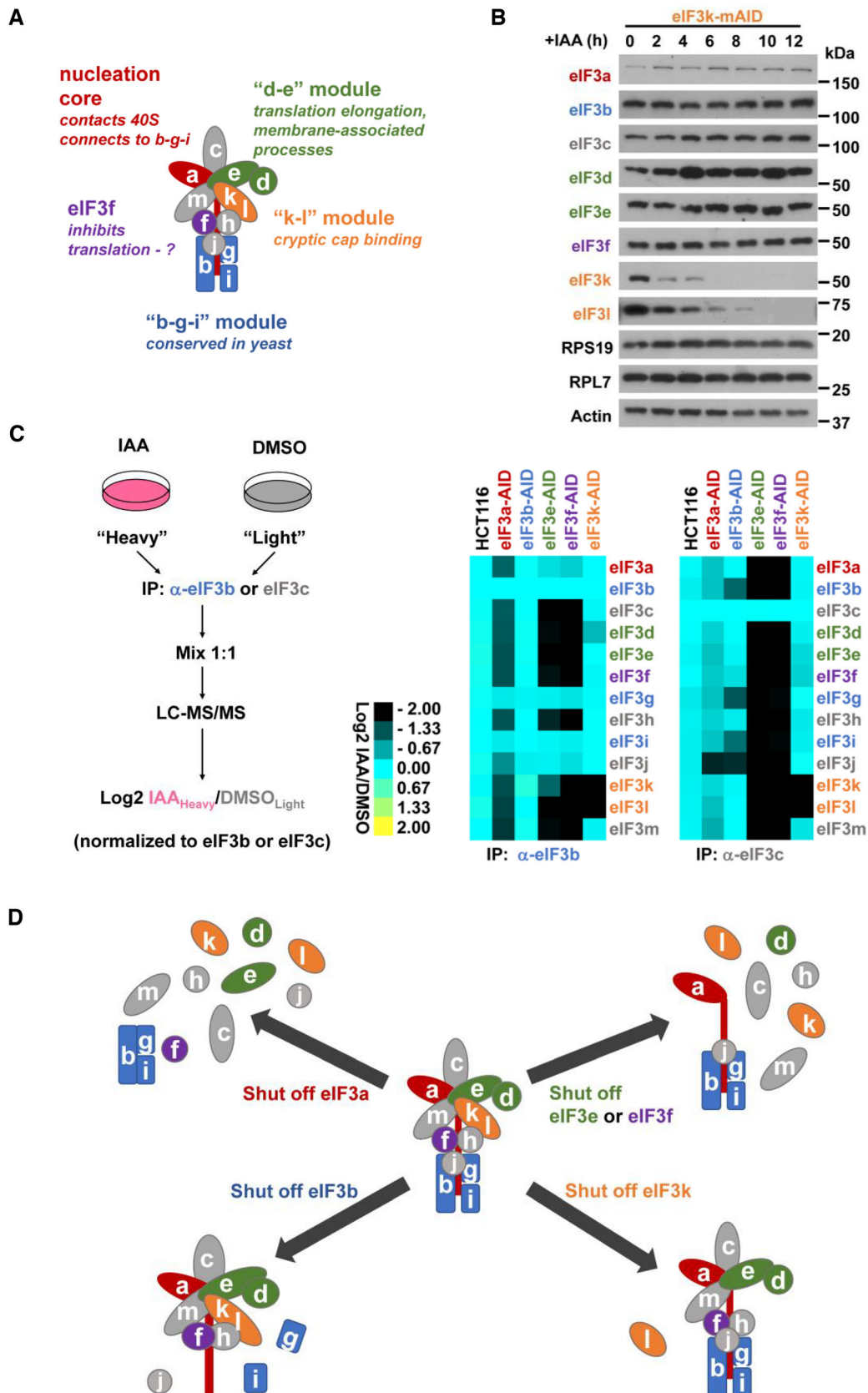


Figure 1.

**Figure 1. Effect of conditional depletion of eIF3 subunits on the eIF3 holo-complex.**

- A Schematic of holo-eIF3 with the five modules targeted for conditional depletion highlighted in different colors.
- B HCT116 cells in which eIF3k was homozygously modified with the mAID domain to trigger auxin-dependent degradation were exposed to 500  $\mu$ M indole-3-acetic acid (IAA) for the periods shown, and cell lysate was subjected to immunoblotting with the indicated antibodies (for quantification see Appendix Fig S1).
- C Analysis of holo-eIF3 complex formation by quantitative SILAC proteomics. eIF3-mAID cell lines were grown either in regular “light” (L) media or in media supplemented with stable “heavy” (H) lysine and arginine. Heavy-labeled cells were treated with IAA for 12 h to shut off the expression of eIF3 subunits. eIF3 was immunopurified from both conditions using antibodies against eIF3b or eIF3c. Upon trypsin digestion, corresponding L (DMSO vehicle control) and H (IAA) samples were mixed and analyzed by LC–MS/MS (left panel). Average changes in H/L ratios were determined, normalized to the bait (eIF3b or eIF3c, respectively), and plotted in a heatmap (right panel).
- D Conceptual graphical summary of the main effects of eIF3 subunit depletion on holo-eIF3 as determined by quantitative proteomics and native PAGE analysis (Fig EV2B).

Source data are available online for this figure.

Lastly, depletion of eIF3k resulted in  $\sim$  80% of eIF3 complexes lacking the eIF3k-l module (Figs 1C and D, and EV2A).

The conclusions drawn from the proteomic analysis were confirmed by native PAGE analysis (Fig EV2B). Here again, depletion of eIF3a led to a stark reduction in the high molecular weight complex co-migrating with holo-eIF3 in parental HCT116 cells as measured with antibodies against eIF3b, c, e, f, k, i, and g. However, in line with the SILAC data, a smaller complex representing the “b-g-i” subcomplex was maintained (Fig EV2B). In contrast, depletion of eIF3k did not appreciably affect the apparent eIF3 holo-complex, a finding that is consistent with the minor impact of loss of the eIF3k-l module on the total mass of the complex. Finally, cells depleted of eIF3e and eIF3f retained substantial amounts of the core complex containing eIF3a, b, g, and i (Fig EV2B). Due to limited resolution, the effect of depletion of eIF3b on holo-eIF3 could not be assessed by native PAGE as the resulting eIF3 octameric core complex (Fig 1C and D) cannot be readily distinguished from holo-eIF3.

In summary, the data obtained with acute depletion of eIF3 subunits showed that removal of individual eIF3 subunits distinctly reshapes eIF3 complex architecture rather than entirely destroying the complex (Fig 1D). This raised the possibility that eIF3 is organized in distinct subunit-specific functional modules.

**Subunit-specific functions of eIF3 in cell proliferation and tumor growth**

To begin to assess module-specific functions, we tested the effect of acute depletion of eIF3 subunits on cell proliferation. Whereas

eIF3a, b, e, and f were equally required for cell proliferation as determined by a surrogate metabolic assay measuring NAD(P)H levels (MTT assay; Fig 2A) as well as colony formation (Fig 2B, Appendix Fig S2A), eIF3k was entirely dispensable for both. In fact, cells depleted of eIF3k showed higher proliferation than the syngeneic controls maintained in the absence of IAA (Fig 2A and B). The rapid depletion system also allowed us to determine the effect of eIF3 subunits on cell cycle dynamics. Re-entry into S phase upon release from a block in G0/G1 induced by serum starvation was greatly impaired in cell lines depleted of eIF3a, b, and e. Whereas depletion of eIF3f had a milder effect on cell cycle re-entry, cells deficient in eIF3k did not show a difference in cell cycle kinetics from cells maintained in the absence of IAA (Fig 2C).

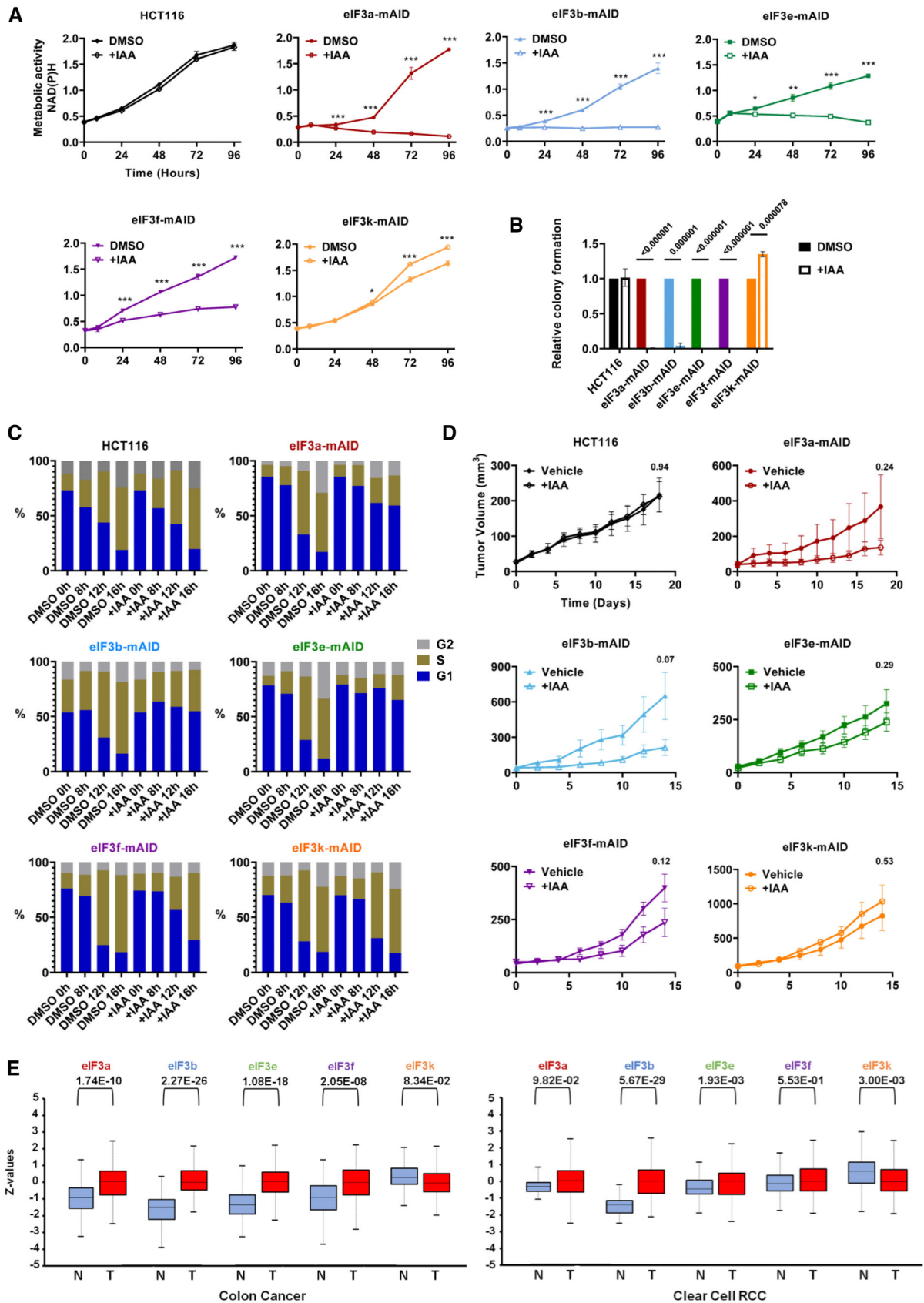
The same differential requirement of eIF3 subunits was observed upon growing the conditional depletion cell lines as xenograft tumors in mice. Once tumors reached a diameter of  $\sim$  4 mm (volume  $\sim$  50 mm<sup>3</sup>), eIF3 subunits were depleted by daily oral gavage of IAA. IAA did not affect the growth of tumors established from parental HCT116 cells relative to the vehicle (Fig 2D, Appendix Fig S2B). Whereas tumor sizes increased in mice treated with the vehicle control, the growth of eIF3a-mAID and eIF3b-mAID tumors was substantially reduced upon administration of IAA. eIF3e-mAID and eIF3f-mAID tumors were also suppressed by IAA, although to a lesser extent. In marked contrast, tumors grew to bigger sizes when eIF3k was depleted (Fig 2D, Appendix Fig S2B), suggesting that eIF3k plays a tumor suppressive role, whereas the other eIF3 subunits examined have pro-tumorigenic function. Consistent with this notion are proteomic data showing that average protein levels of

**Figure 2. Effect of depletion of eIF3 subunits on cell and tumor growth.**

- A Parental HCT116 and the five different conditional eIF3-mAID cell lines were treated with the vehicle DMSO or with IAA for the periods indicated. Metabolic activity (i.e., NAD(P)H) as a proxy of cell proliferation was determined by MTT assay. Graphs represent means  $\pm$  SD,  $n = 5-6$ . Asterisks denote: \* $P < 0.005$ , \*\* $P < 0.00005$ , \*\*\* $P < 0.000005$  (two-stage step-up method of Benjamini, Krieger, and Yekutieli).
- B  $1 \times 10^3$  cells of the indicated cell lines were plated and grown in DMSO or IAA for 2 weeks. Colony numbers were counted and are shown in a bar graph relative to the DMSO-treated control. Note that very low numbers of colonies were obtained for IAA-treated eIF3a-mAID, eIF3e-mAID and eIF3f-mAID – hence no bars are visible. Bars represent means  $\pm$  SD,  $n = 3$ . Numbers indicate  $P$ -values (unpaired Student's  $t$ -test).
- C The indicated cell lines were subjected to serum withdrawal (0% FBS) for 16 h. DMSO or IAA was added and cells were stimulated to re-enter the cell cycle by refeeding with media containing 10% FBS. Cells were fixed after the indicated time points, and the cellular DNA content was measured by flow cytometry. Data are representative of 2 (HCT116, eIF3a-mAID, eIF3b-mAID) or 3 (eIF3e-mAID, eIF3f-mAID, eIF3k-mAID) experiments.
- D  $1 \times 10^6$  eIF3-mAID cells were injected into nude mice. When tumors reached a diameter of  $\sim$  4 mm, mice were treated with vehicle or 500 mg/kg IAA, and tumor growth was measured for 2 weeks. Graphs represent means  $\pm$  SD,  $n = 5-7$ . Numbers indicate  $P$ -values (two-stage step-up method of Benjamini, Krieger, and Yekutieli).
- E Expression of the indicated eIF3 proteins in 97 colon adenocarcinomas versus 100 normal colonic mucosae and 110 clear cell renal cell carcinomas versus 84 normal kidney samples. Log<sub>2</sub> spectral count data from CPTAC (Chen et al., 2019) via UALCAN portal (Chandrashekar et al., 2022).

Data information: The median (50<sup>th</sup> percentile), 25<sup>th</sup> percentile (lower box), 75<sup>th</sup> percentile (upper box), 5<sup>th</sup> percentile (lower whisker), and 95<sup>th</sup> percentile (upper whisker) are indicated.  $n =$  biologically independent tumor samples.

Source data are available online for this figure.





eIF3a, b, e, and f were upregulated in human colon and renal cancers, whereas eIF3k protein was downregulated (Fig 2E).

### mRNA selectivity of eIF3 subunits revealed by ribonomic and proteomic profiling

To determine the effect of acute depletion of eIF3 subunits on global mRNA translation, we performed sucrose density gradient fractionation to separate actively translating polysomes (P) from 40S, 60S, and 80S monosomes (M). Addition of IAA to the various cell lines for 12 h led to ~72–90% depletion of eIF3 subunits (Figs 3A and EV3A). Whereas IAA did not affect the P/M ratio of parental HCT116 cells, depletion of eIF3a, e, and f subunits led to substantial decreases in the P/M ratios indicating substantial inhibition of translation with eIF3a depletion showing the most pronounced effect (Figs 3B and EV3B). Addition of IAA to eIF3b-mAID cells for 12 h did not affect the P/M ratio even so eIF3b was 73% depleted (Fig 3A and B, Appendix Fig S3A). Only ~90% depletion of eIF3b after 24 h of IAA treatment led to a decrease in translation (Appendix Fig S3A). In contrast, depletion of eIF3k did not decrease translation but rather caused a 6% ( $\pm 2.7\%$ ) increase in the P/M ratio, a finding consistent with a previous study (Herrmannová *et al*, 2020) and with the increased cell proliferation and tumor growth observed with the eIF3k-mAID cell line (Fig 2).

To assess translation of individual mRNAs upon depletion of eIF3 subunits, we performed RNA-seq of triplicate samples of mRNA contained in sucrose density gradient fractions corresponding to > 2 polyribosomes (polysomal mRNA). In parallel, we sequenced triplicate samples of total cellular mRNA and compared the data to the polysomal mRNA-seq (analysis strategy illustrated in Fig EV3C, all data in Datasets EV1 and EV2). As shown in a scatterplot of Log2 fold changes of polysomal mRNA versus Log2 fold changes of total mRNA, IAA treatment for 12 h did not lead to any significant changes (FDR  $\leq 0.05$ ) in polysomal mRNA of parental HCT116 cells, and only 6 mRNAs were changed in the total RNA sample (Figs 3C and EV3D). Similarly, the eIF3b-mAID cell line showed a small number of changes in polysomal fractions (22 mRNAs), an observation that is consistent with the unchanged P/M ratio after 12 h of IAA administration (Fig 3B, Appendix Fig S3A). One hundred and fifty-two mRNAs were changed in the total mRNA sample indicating

a distinct transcriptional response to short-term eIF3b depletion (Fig EV3D).

In contrast, depletion of eIF3a for 12 h led to a pronounced downregulation of 5,049 polysomal mRNAs (Figs 3C and EV3D). Only 1.58% of these changes also registered in the total mRNA sample, indicating that the vast majority of the changes occurred at the translational level. Depletion of eIF3a also led to the induction of 328 mRNAs in the total mRNA sample but only 26 (7.9%) of these mRNAs were significantly increased in the polysomal mRNA sample (Fig EV3D). This indicates that cells acutely depleted of eIF3a mount a transcriptional response, which fails to substantially perpetuate into protein production after 12 h of eIF3a depletion.

Cells depleted of eIF3e or eIF3f showed similar albeit blunted responses. 2,561 mRNAs were downregulated in polysomes of eIF3e-depleted cells of which 5% were also downregulated in the total mRNA sample. In eIF3f-depleted cells, 1,058 mRNAs were reduced in the polysomal fraction, and 1.7% of these changes were reflected in the total mRNA sample (Figs 3C and EV3D). These differences in numbers are consistent with the less pronounced growth phenotypes of cells depleted of eIF3f compared with eIF3e (Fig 2A and C). In stark contrast, in eIF3k-depleted cells, only eight mRNAs were downregulated in polysomes, whereas 155 mRNAs were upregulated and only 3.2% of these changes occurred in the total mRNA sample (Figs 3C and EV3D).

Interrogating the polysomal changes for overrepresented Gene Ontology terms, no functional enrichments were obtained for eIF3a-depleted cells. This indicates that eIF3a promotes the translation of a wide array of mRNAs without any detectable selectivity. Likewise, there was no enrichment for eIF3b-depleted cells due to the low number of mRNAs affected 12 h after IAA. In contrast, depletion of eIF3e and eIF3f led to enrichment of an overlapping set of functional categories, including ribosomes, mitochondrial organization, and membrane processes in the sets of mRNAs whose polysomal association was decreased (Fig 3D, Dataset EV3). These categories agree with those identified in our previous studies in yeast and MCF10A cells (Shah *et al*, 2016, 3; Lin *et al*, 2020, 3). In contrast, the GO terms “ribosomal subunit” and “polysome” were enriched in the set of 155 mRNA which increased in the polysomal fraction upon depletion of eIF3k, suggesting a role of eIF3k in regulating ribosome biosynthesis (Fig 3D, Dataset EV3).

### Figure 3. Effect of depletion of eIF3 subunits on mRNA translation.

- The indicated conditional eIF3 cell lines were exposed to 500  $\mu$ M IAA for 12 h to induce the degradation of the respective eIF3 subunits. Cell lysates were subjected to immunoblotting to quantify the expression of the indicated eIF3 subunits. Signals were normalized to the reference signal of actin and plotted relative to the vehicle DMSO. Bars represent means  $\pm$  SD,  $n = 3$ . Numbers indicate  $P$ -values (unpaired Student's  $t$ -test).
- The indicated cell lines were exposed to IAA for 12 h, and cell lysates were separated by sucrose density gradient centrifugation. The monosomal (M) and polysomal (P) peaks were quantified, and P/M ratios relative to the vehicle DMSO were plotted. Bars represent means  $\pm$  SD,  $n = 3$ . Numbers indicate  $P$ -values (unpaired Student's  $t$ -test).
- Scatter plots of changes in polysomal mRNA versus total mRNA upon depletion of the indicated eIF3 subunits.
- Enrichment of Gene Ontology terms in the sets of polysome-associated mRNAs decreased in the polysomal fractions of eIF3f- or eIF3e-depleted cells or increased in eIF3k-depleted cells.
- Distribution histograms of translational efficiencies (TEs) of the mRNA sets shown in (C). The total number of mRNAs and the median TE of each dataset are indicated. The number of up and down changes with FDR  $\leq 0.2$  as well as the median of all changed items are indicated in red, blue, and black bold print.
- Distribution histograms of the protein synthesis ratios determined in eIF3 subunit depleted versus replete cells. The total number of measured proteins and the median synthesis change of each dataset are indicated. The number of up and down changes with FDR  $\leq 0.1$  as well as the median of all changed items are indicated in red and blue print.

Data information:  $n$  = number of biological replicates.  
Source data are available online for this figure.

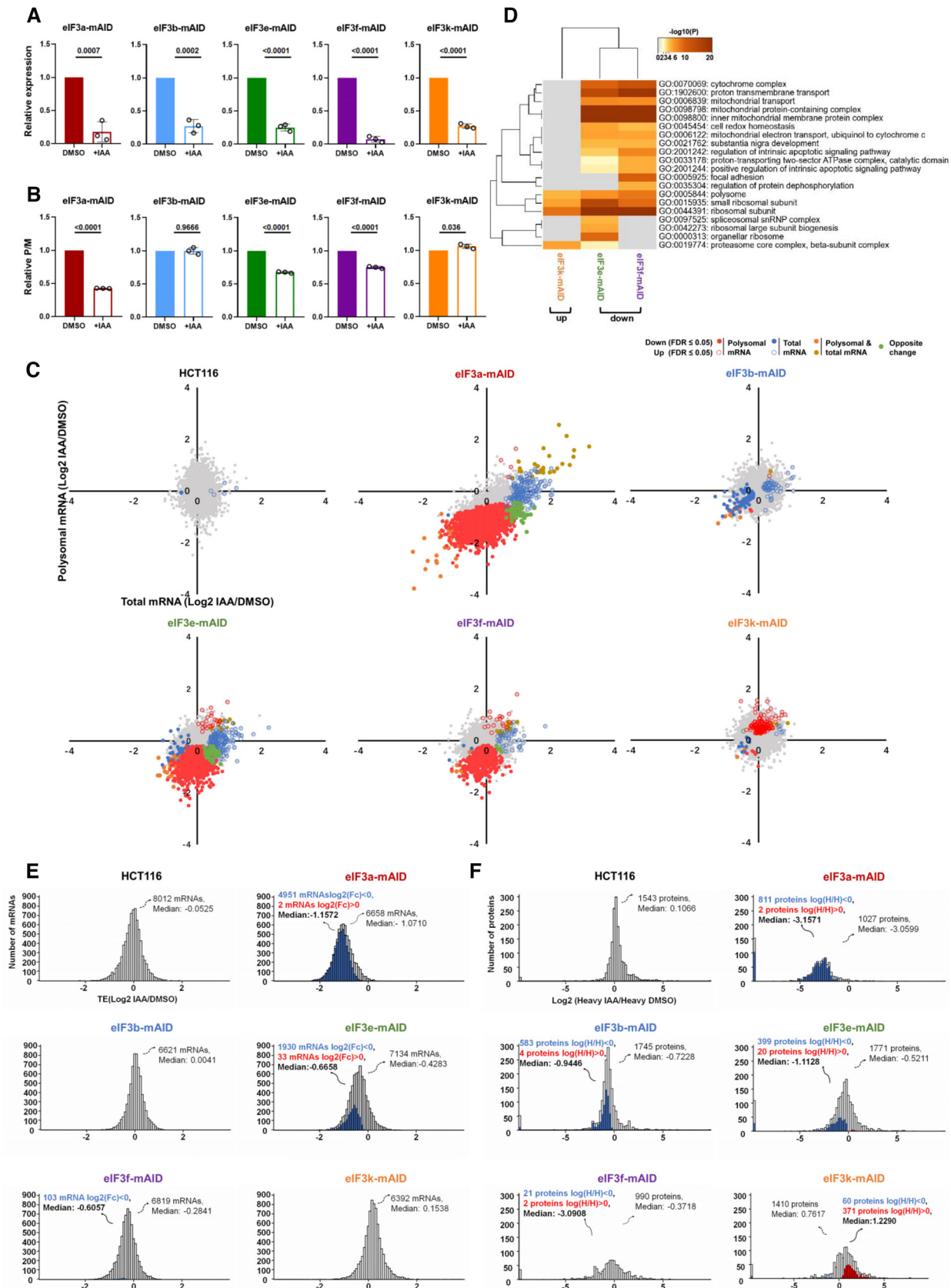


Figure 3.

We also calculated translational efficiencies (TEs) defined as  $\text{Log}_2$  polysomal mRNA / total mRNA (Dataset EV4). As expected, median TEs were centered closely around 0 for parental HCT116 and eIF3b-mAID cells after 12 h of IAA (Fig 3E). TE fold change medians were strongly reduced for eIF3a ( $\text{Log}_2\text{TE} = -1.07$ ), eIF3e ( $\text{Log}_2\text{TE} = -0.43$ ) and eIF3f ( $\text{Log}_2\text{TE} = -0.28$ ) depleted cells but increased for eIF3k-depleted cells ( $\text{Log}_2\text{TE} = 0.15$ ) (Fig 3E). The number of mRNAs whose TE changed (defined as changes at  $\text{FDR} \leq 0.2$ ) in the various cell lines correlated with the overall effect size on mRNA translation and ranged from 4,951 mRNAs in eIF3a-depleted cells to 1930, 103, and 0 in eIF3e-, eIF3f-, and eIF3k-depleted cells, respectively. The low number of TE changes in eIF3f- and eIF3k-depleted cells is due to the comparatively small effect size on translation which we could not measure reliably.

A potential limitation of extrapolating mRNA translation from the RNA-seq data is that co-fractionation with polyribosomes does not necessarily indicate that an mRNA is actively translated. We therefore performed an orthogonal analysis of protein synthesis by metabolic pulse labeling with heavy amino acids and protein identification by LC-MS/MS (pSILAC, Selbach *et al*, 2008). Six hours after the addition of IAA or the vehicle DMSO, eIF3-mAID cells were labeled with heavy ( $^{13}\text{C}$   $^{15}\text{N}$ ) lysine and arginine for another 6 h and, as with the RNA-seq experiments, cells were harvested for LC-MS/MS after a total of 12 h in IAA.  $\text{Log}_2$  fold changes (Heavy IAA/Heavy DMSO) in the labeling of eIF3 proficient and depleted cells with heavy amino acids were determined to assess eIF3 subunit-dependent differences in protein synthesis (Dataset EV5). Between 990 and 1771 proteins were measured in the various cell lines. Data for 1,543 proteins from parental HCT116 cells showed that protein synthesis was not perturbed by IAA treatment with not a single protein differing at the FDR cutoff of 0.1 and the  $\text{Log}_2$  median fold change ( $\text{Log}_2\text{pSILAC}$ ) centered narrowly around 0 (Fig 3F).

In stark contrast, the synthesis of 811 out of the total of 1,027 proteins measured (79%) showed a reduction in eIF3a-depleted cells for a median  $\text{Log}_2$  fold change of -3.16 (Fig 3F). Similar albeit weaker reductions were measured upon depletion of eIF3e (median  $\text{Log}_2\text{pSILAC} = -0.52$ , 22.5% of measured proteins synthesis rates decreasing) and eIF3f (median  $\text{Log}_2\text{pSILAC} = -0.37$ , 2.1% of synthesis rates decreasing; Fig 3F).

Surprisingly, protein synthesis was also downregulated in eIF3b-mAID cells 12 h after addition of IAA (median  $\text{Log}_2\text{pSILAC} = -0.72$ , Fig 3F) even so polysome profiles and translation efficiency (median  $\text{Log}_2\text{TE} = 0.0041$ ) were unchanged at the same time point (Fig 3B, Appendix Fig S3A). Among the 81 mRNAs downregulated in the total but not the polysomal mRNA sample upon treating eIF3b-mAID cells with IAA for 12 h, we noticed a strong enrichment of the GO terms “cellular amino acid metabolic process” and “organic acid transport” (Appendix Fig S3B). Manual inspection revealed the downregulation of several mRNAs encoding amino acid transporters. These included SLC7A5 and SLC38A2 transporting neutral amino acids as well as SLC7A1 mediating the import of positively charged lysine and arginine, which were used for stable isotope labeling in the pSILAC experiment. We confirmed 13–30% downregulation of these amino acid transporter mRNAs in total mRNA by qPCR but not in polysomal mRNA fractions (Appendix Fig S3C and D). Thus, apparent downregulation of mRNAs encoding amino acid transporters at the transcriptional level is most likely responsible for the reduction in

protein synthesis observed upon shutoff of eIF3b protein expression for 12 h.

In agreement with the RNA-seq-based TE, protein synthesis was increased in eIF3k-depleted cells rather than decreased (median  $\text{Log}_2\text{pSILAC} = 1.23$ , 26% of synthesis rates increased, Fig 3F). Global agreement between RNA-seq (TE) and protein synthesis (pSILAC) data moving into the same directions was obtained for all eIF3 conditional cell lines with the exception of eIF3b-mAID as expected (Appendix Fig S4).

### eIF3k negatively modulates global protein synthesis through suppressing ribosomal protein synthesis

The most striking contrast between eIF3 subunits was the unique upregulation of cell and tumor growth and global translation in eIF3k-depleted cells (Figs 2 and 3), whereas cells depleted of all other eIF3 subunits showed the opposite behavior. We first considered the possibility that depletion of eIF3k causes increased growth by sensitizing cells to mitogenic signaling. To test this, we asked whether the growth advantage of eIF3k-depleted cells would be enhanced at reduced concentrations of fetal bovine serum (FBS), thus indicating increased mitogen sensitivity. Reducing FBS from 10 to 5% or 2% did not lead to a greater advantage of eIF3k-depleted cells (Fig 4A). Instead, eIF3k replete and depleted cells maintained their characteristic difference in cell number increase over time, which was also reflected in the metabolic assay measuring NAD(P)H levels (CCK-8, Appendix Fig S5A). We also did not observe any differences in serum stimulated mitogenic signaling with mTOR, S6 kinase, and Erk1/2 phosphorylation being induced with similar kinetics in eIF3k replete and depleted cells (Fig 4B, Appendix Fig S5B), findings that are consistent with the cell cycle kinetics in Fig 2C. Likewise, cells showed no difference in sensitivity to the mTOR inhibitor rapamycin depending on eIF3k status as determined by immunoblotting with phosphospecific mTOR antibodies (Fig 4C, Appendix Fig S5C). We did note a distinct increase in phosphorylated S6 kinase in eIF3k-depleted cells (Fig 4C, Appendix Fig S5C), suggesting that ribosome activity may be increased. In summary, these data suggest that increased growth of eIF3k-depleted cells is not due to increased responsiveness to mitogenic stimulation.

Since ribosome capacity is limiting for growth (Dai & Zhu, 2020), increased ribosome synthesis as apparent from the GO term enrichment (Fig 3D) might explain enhanced cell and tumor growth of eIF3k-depleted cells. Indeed, as judged by sucrose density gradient profiling of lysate prepared from an equal number of cells, depletion of eIF3k for 12 or 48 h led to a 6.5–6.9% ( $P < 0.005$ ) increase in total cellular ribosome content (Fig 5A, Appendix Fig S6A). RT-qPCR quantification of ribosomal RNA in sucrose density gradient fractions revealed a 43.08% ( $P = 0.045$ ) increase in 18S rRNA and a 17.71% ( $P = 0.249$ ) increase in 28S rRNA in eIF3k-depleted cells (Fig 5B). In line with the GO term enrichment analysis, inspection of the global transcriptomic and proteomic eIF3k-mAID datasets revealed a list of 12 ribosomal proteins (RPs) whose mRNAs were significantly upregulated in polysomal RNA ( $\text{FDR} < 0.05$ ) but not in the total mRNA, thus having an increased TE (Dataset EV6). The corresponding proteins also showed increased synthesis by pSILAC (Dataset EV6). Surveying our data on all 75 RPs detected, we found 95% of them upregulated in polysomal mRNA and having increased TE in eIF3k-depleted cells (Appendix Fig S6B–D). The majority of



RPs also showed increased synthesis by pSILAC (Appendix Fig S6E). To directly quantify cellular ribosome content, we performed quantitative LC-MS/MS analysis of polysomal fractions and found that 85% of RPs were increased in eIF3k-depleted cells for an average 1.32-fold upregulation (Appendix Fig S6F). Thus,

depletion of eIF3k causes an increase in total ribosome content along with increased cell proliferation.

We chose three RP-encoding mRNAs, *RPS15A* (*uS8*), *RPS4X* (*eS4*), and *RPL7A* (*eL8*) to determine their partitioning into monosomal and polysomal mRNA fractions by RT-qPCR. Triplicate

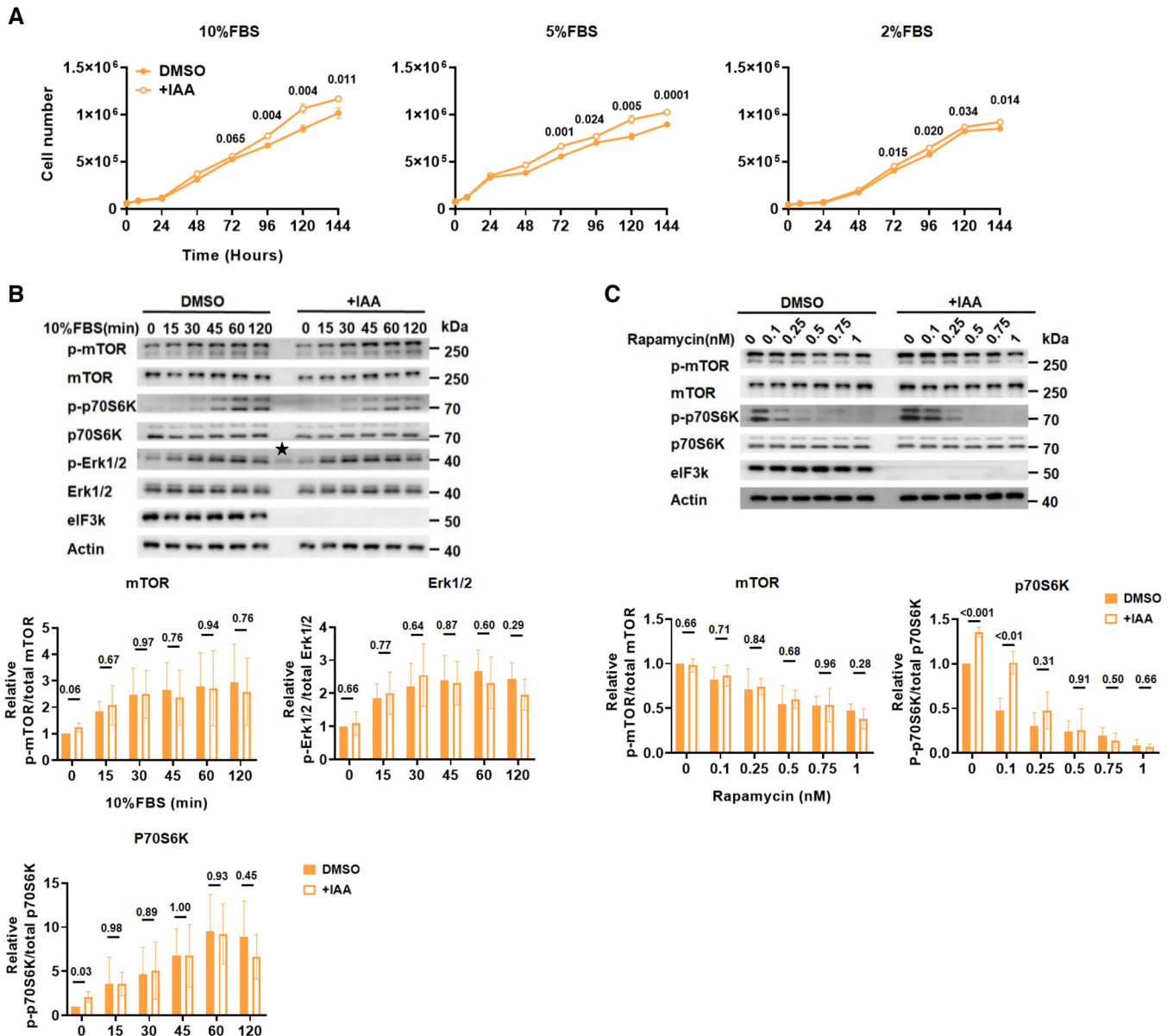


**Figure 4. Effect of eIF3k depletion on growth factor sensitivity.**

- A** eIF3k-mAID cells were maintained in media containing different concentrations of FBS and DMSO or IAA as indicated, and cell numbers were determined at various time points. Data represent means  $\pm$  SD,  $n = 3$  biological replicates. Numbers indicate  $P$ -values (two-stage step-up method of Benjamini, Krieger, and Yekutieli).
- B** eIF3k-mAID cells were serum starved by maintaining in media containing 0% FBS for 24 h. During the last 12 h of starvation, DMSO or IAA was added as indicated. Cells were restimulated with media containing 10% FBS, and the expression of the indicated proteins was followed over a period of 120 min. The data from triplicate experiments were quantified and plotted as relative ratios of phosphorylated to unphosphorylated species. Bars represent means  $\pm$  SD,  $n = 3$  (see Appendix Fig S5B). Numbers indicate  $P$ -values (unpaired Student's  $t$ -test).
- C** eIF3k-mAID cells were exposed to IAA or DMSO for 12 h, followed by the addition of increasing concentrations of rapamycin for 1 h. The expression of the indicated proteins was determined by immunoblotting. The data from triplicate experiments were quantified and plotted as relative ratios of phosphorylated to unphosphorylated species. Bars represent means  $\pm$  SD,  $n = 3$  (see Appendix Fig S5C). Numbers indicate  $P$ -values (unpaired Student's  $t$ -test).

Source data are available online for this figure.

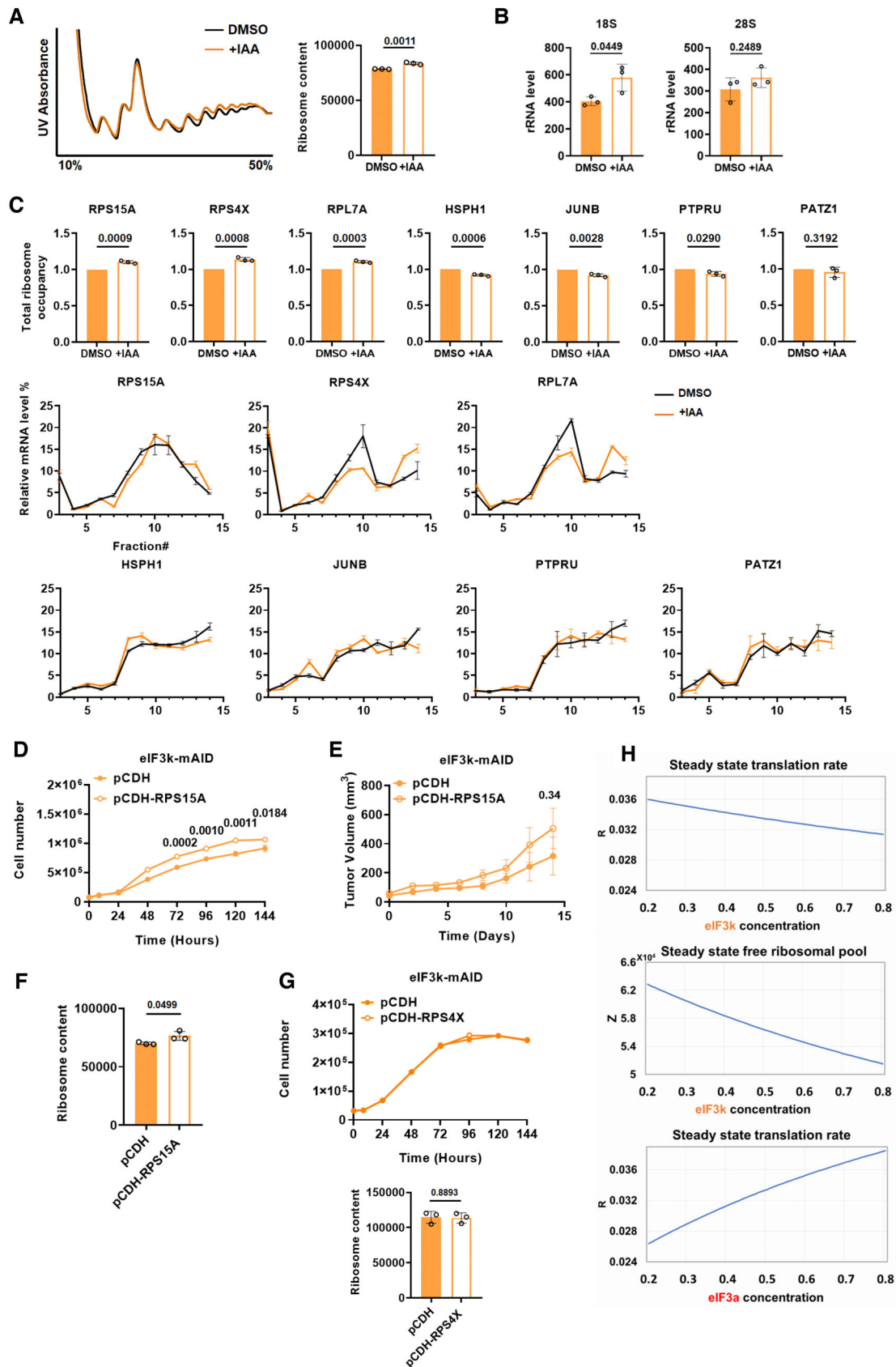


Figure 5.

**Figure 5. Effect of eIF3k depletion on ribosome content and RPS15A.**

- A Lysates of eIF3k-mAID cells exposed to DMSO or IAA for 12 h were separated by sucrose density gradient centrifugation. Total ribosome content was determined by integrating the monosomal and polysomal peaks and plotted. Error bars represent means  $\pm$  SD,  $n = 3$ . Numbers indicate  $P$ -values (unpaired Student's  $t$ -test).
- B 18S and 28S rRNA levels were determined by RT-qPCR across a sucrose density gradient. Bars represent mean rRNA levels in summed monosomal and polysomal fractions  $\pm$  SD,  $n = 3$ ; numbers indicate  $P$ -values (unpaired Student's  $t$ -test).
- C Total ribosome occupancy of the indicated mRNAs in eIF3k-mAID cells exposed to DMSO or IAA for 12 h was determined by RT-qPCR of RNA across a sucrose density gradient (see [Materials and Methods](#)). Bars represent means  $\pm$  SD,  $n = 3$ ; numbers indicate  $P$ -values (unpaired Student's  $t$ -test). Triplicate RT-qPCR data across the sucrose gradient are shown below the bar graphs.
- D Equal numbers of eIF3k-mAID cells stably expressing ectopic RPS15A (pCDH-RPS15A) or empty vector (pCDH) were plated and counted over a period of 6 days. Graphs represent means  $\pm$  SD,  $n = 3$ . Numbers indicate  $P$ -values (two-stage step-up method of Benjamini, Krieger, and Yekutieli).
- E  $1 \times 10^6$  eIF3k-mAID cells stably expressing ectopic RPS15A (pCDH-RPS15A) or empty vector (pCDH) were injected into nude mice and tumor growth was followed for 2 weeks. Graphs represent means  $\pm$  SD,  $n = 5-7$  (see [Fig EV4B](#)). Numbers indicate  $P$ -values (two-stage step-up method of Benjamini, Krieger, and Yekutieli).
- F Lysate of eIF3k-mAID cells stably expressing ectopic RPS15A (pCDH-RPS15A) or empty vector (pCDH) were separated by sucrose density gradient centrifugation. Total ribosome content was determined by integrating and summing the monosomal and polysomal peak areas. Error bars represent means  $\pm$  SD,  $n = 3$ . Numbers indicate  $P$ -values (unpaired Student's  $t$ -test).
- G Equal numbers of eIF3k-mAID cells stably expressing ectopic RPS4X (pCDH-RPS4X) or empty vector (pCDH) were plated and counted over a period of 6 days. Graphs represent means  $\pm$  SD,  $n = 3$ . Numbers indicate  $P$ -values (two-stage step-up method of Benjamini, Krieger, and Yekutieli). Total ribosome content of these cells was determined as described in (A).
- H Steady-state free ribosomal pool and translation rate as a function of eIF3k concentration (top two graphs) and the steady-state translation rate as a function of eIF3a concentration (bottom graph). The concentration of other eIF3 subunits is kept constant at 0.5.
- Data information:  $n$  = number of biological replicates.  
Source data are available online for this figure.

experiments confirmed increased polysomal association of RP-encoding mRNAs 12 h after adding IAA to eIF3k-mAID cells, while no such increase was seen for eIF3k-independent *PATZ1*, *PTPRU*, *JUNB*, and *HSPH1* mRNAs ([Fig 5C](#)). Similar results were obtained after extending eIF3k depletion to 48 h ([Fig EV4A](#)). The data strongly suggest that RP mRNAs are targets of negative translational control by eIF3k.

RPS15A is special because it is frequently overexpressed in human colorectal cancers ([Chen et al, 2016](#)), and its overexpression was shown to be sufficient to promote tumor growth in mice, although its effects on translation were not assessed ([Guo et al, 2018](#); [Liu et al, 2019](#)). We found that stable overexpression of *RPS15A* mimicked the effect of eIF3k depletion on cell growth, leading to a marked stimulation ([Fig 5D](#)). Likewise, *RPS15A* overexpression was sufficient to increase tumor growth ([Figs 5E and EV4B](#)) and the total cellular ribosome content ([Fig 5F](#)). No stimulation of cell growth and ribosome content was obtained upon ectopic expression of *RPS4X* ([Fig 5G](#)). These data suggest that depletion of eIF3k promotes cell and tumor growth by increasing cellular ribosome content.

To gauge the plausibility of this conjecture, we sought to integrate our experimental data into a mathematical-computational predictive model. We adopted our previously developed ribosome flow model ([Reuveni et al, 2011](#); [Zarai & Tuller, 2018](#)) that captures fundamental aspects of translation, including (i) potential differences in decoding time for each codon, which is related to the local biophysical properties of the mRNA (e.g., its folding and the encoded amino acids) and its interaction with translation factors and/or the availability of such factors (e.g., tRNA levels); (ii) initiation rates, which are affected by the properties of the mRNA and initiation factors as well as global factors such as the concentrations of ribosomes and translation factors; (iii) multiple ribosomes translating the same mRNA at a certain point in time; (iv) excluded volume interactions between ribosomes and possible traffic jams; (v) directionality of the ribosome flow (the flow is totally asymmetric, i.e., unidirectional); (vi) the fact that mRNA molecules compete for a finite pool of ribosomes. Based on parameters derived

from ribosome foot printing data of HEK293 cells ([Dana & Tuller, 2015](#)), the model can predict the exact relations between the levels of distinct eIF3 subunits and global translation variables such as translation rates and the free ribosomal pool, which are expected to be positively correlated with growth rate. Using TP53 as a model mRNA, we simulated the effect of the eIF3k concentration on the free ribosomal pool and the translation rate, as well as the effect of the eIF3a concentration on the translation rate. As apparent in [Fig 5H](#), decreasing the eIF3k concentration increases the steady-state free ribosomal pool, which in turn increases the translation rate. In contrast, decreasing eIF3a concentration decreases the steady-state translation rate via its effect on initiation. Similar results were obtained for simulating steady-state average ribosome density ( $\rho$ ) and steady-state average ribosome jams ( $\theta$ ) ([Fig EV4C](#)). At the nominal value of concentration 0.5, the model predicts that an 80% depletion of eIF3k results in a 13.4% increase in the steady-state free ribosomal pool ([Fig EV4D](#)), a prediction that approximates the experimental data. Thus, the simulations readily capture key experimental observations of our study: (i) eIF3k has a negative effect on the ribosome pool, and thus on the global initiation rate, translation rate, and growth. (ii) eIF3a positively affects the translation rate via initiation.

#### eIF3k-dependent suppression of RPS15A mRNA translation is mediated by eIF3 binding to the 5'-UTR

Our results suggested that eIF3k is a negative modulator of the translation of RP mRNAs, especially *RPS15A*. To address mechanisms of this regulation, we examined global CLIP datasets ([Lee et al, 2015](#); [Meyer et al, 2015](#)) for the presence of eIF3-binding sites in *RPS15A* and *RPS4X* ([Fig 6A](#)). To assess the requirement of these binding sites for the translation of *RPS15A* and *RPS4X* mRNAs, we performed CRISPR/Cas9 genome editing to delete the binding sites from both alleles of eIF3k-mAID cells. We could not obtain viable cells upon editing *RPS4X*. We subsequently determined by long-read RNA sequencing that the mapped eIF3-binding site is only present in a minor isoform of *RPS4X* mRNA (~5% of the total pool in

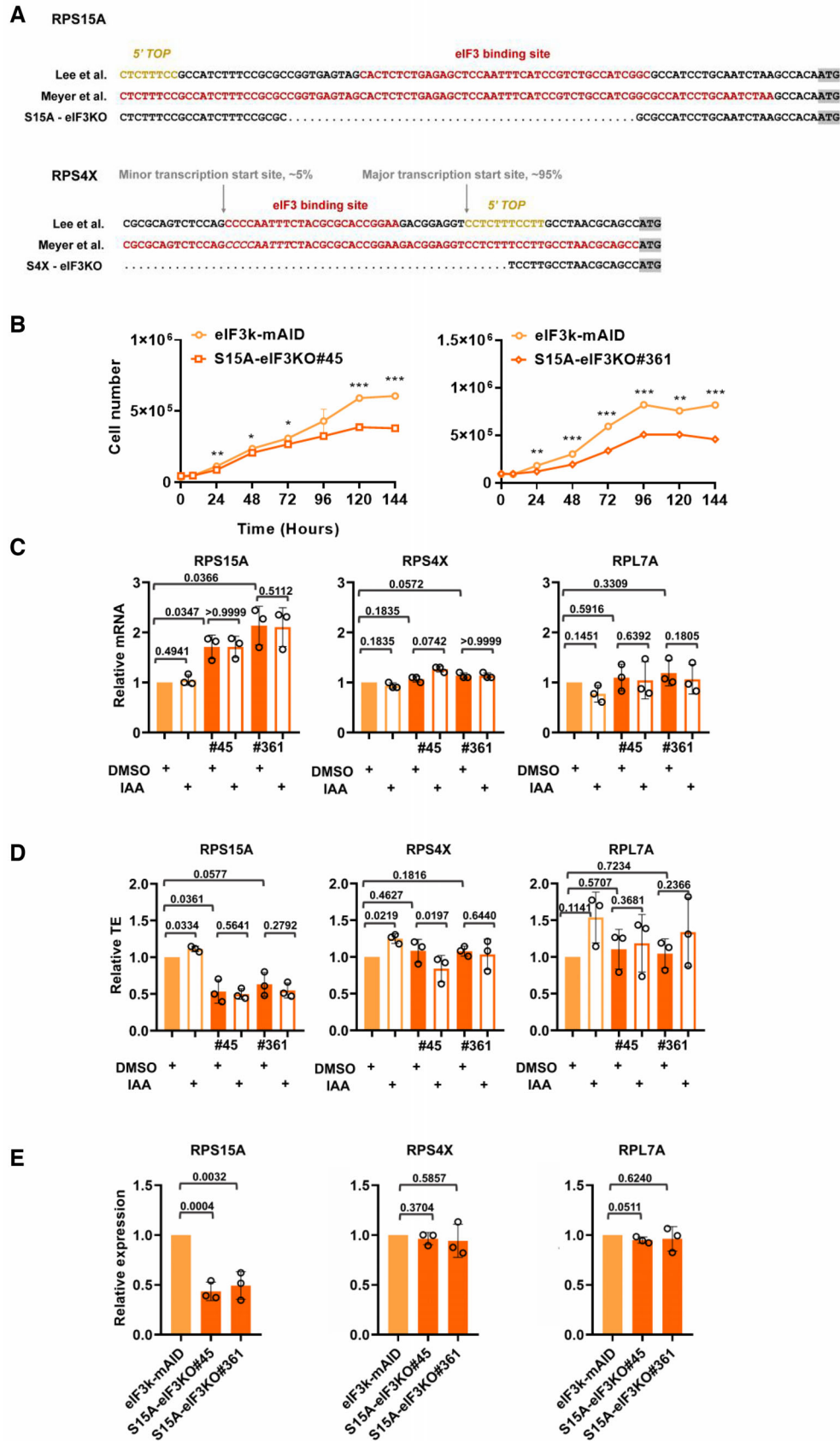


Figure 6.



**Figure 6. Effect of the eIF3-binding site on cell proliferation and RPS15A.**

- A 5'-UTR sequences of RPS15A and RPS4X. 5'-TOP element known to boost translation of ribosomal protein mRNAs (Meyuhas, 2000) are highlighted in gold prints, the eIF3-binding sites mapped by Lee et al (2015) and Meyer et al (2015) are highlighted in red print. The alleles created by gene editing are shown (S15A-eIF3KO, S4X-eIF3KO). Note that the eIF3-binding site in RPS4X is upstream of or overlapping with the major transcription start site. Thus, the S4X-eIF3KO truncation we failed to generate most likely abolished the transcription of RPS4X mRNA.
- B Parental eIF3k-mAID cells or S15A-eIF3KO cells (clones #45 and #361) were maintained in standard media, and cell numbers were determined at various time points. Data represent means  $\pm$  SD,  $n = 3$ . Asterisks denote: \* $P < 0.005$ , \*\* $P < 0.00005$ , \*\*\* $P < 0.000005$  (two-stage step-up method of Benjamini, Krieger, and Yekutieli).
- C Relative levels of mRNAs encoding RPS15A, RPS4X, and RPL7A before and after depletion of eIF3k were determined in the indicated cell lines by RT-qPCR. Data were normalized to the signal obtained for GAPDH. Bars represent means  $\pm$  SD,  $n = 3$ ; numbers indicate  $P$ -values (unpaired Student's  $t$ -test).
- D Relative translational efficiencies (TEs) of mRNAs encoding RPS15A, RPS4X, and RPL7A before and after depletion of eIF3k were determined in the indicated cell lines. RT-qPCR was performed on total RNA and on RNA contained within polysomal fractions  $> 2$  ribosomes, and TE was calculated according to the formula TE = polysomal mRNA / total mRNA. Bars represent means  $\pm$  SD,  $n = 3$ ; numbers indicate  $P$ -values (unpaired Student's  $t$ -test).
- E Basal expression of the indicated proteins was determined in parental eIF3k-mAID cells or S15A-eIF3KO cells (clones #45 and #361) by immunoblotting, followed by quantification of the blots. Bars represent means  $\pm$  SD,  $n = 3$  (Fig EV5A). Numbers indicate  $P$ -values (unpaired Student's  $t$ -test).

Data information:  $n$  = number of biological replicates.

Source data are available online for this figure.

human lymphocytes, Fig 6A). Genomic deletion of the eIF3-binding site is predicted to disrupt the promoter of the major mRNA species, thus likely abolishing the transcription of  $\sim 95\%$  of the RPS4X mRNA and leading to lethality. This does not rule out a role of the eIF3-binding site in increasing the translation of the minor isoform of RPS4X mRNA in eIF3k-depleted cells, but this cannot be addressed by genomic deletion of the mapped binding site.

RPS15A 5'-UTR edited cell lines were obtained, however, which were denoted S15A-eIF3KO clones #45 and #361. While the edited cells grew slower than the parental eIF3k-mAID cells (Fig 6B), they had  $\sim 2$ -fold increased RPS15A but not RPS4X or RPL7A mRNA levels (Fig 6C). However, TE of RPS15A mRNA was  $\sim 2$ -fold lower in the 5'-UTR edited cell lines (Fig 6D), observations that were consistent with a 2-fold reduction in RPS15A but not RPS4X or RPL7A protein (Figs 6E and EV5A). These data indicate that the eIF3-binding site in the 5'-UTR of the RPS15A mRNA acts as an amplifier of RPS15A mRNA translation. eIF3k and eIF3l were also reduced in S15A-eIF3KO cells, possibly as a compensatory measure aimed at boosting RPS15A translation (Fig EV5A).

Despite these baseline changes, S15A-eIF3KO cells depleted for eIF3k did not show the increase in growth rate found in the parental eIF3k-mAID cells (Fig 7A). Likewise, the growth of tumors derived from S15A-eIF3KO cells was not stimulated upon eIF3k depletion (Fig 7B). In agreement with these growth phenotypes,

eIF3k-depleted S15A-eIF3KO cells did not show an increase in total ribosome content (Figs 7C and EV5B). Unlike in parental eIF3k-mAID cells, depletion of eIF3k in S15A-eIF3KO cells did not lead to increased recruitment of RPS15A mRNA into polysomes, whereas the stimulation was largely maintained for RPS4X and RPL7A mRNAs (Figs 7D and EV5C). Likewise, the increase in the TE of RPS15A mRNA observed in eIF3k-depleted parental cells was not apparent in 5'-UTR edited S15A-eIF3KO cells (Fig 6D). Finally, RNA immunoprecipitation with eIF3c antibodies showed that binding of eIF3 to RPS15A mRNA was diminished in S15A-eIF3KO cells but increased in eIF3k-mAID cells upon downregulation of eIF3k (Fig 7E). Importantly, ectopic expression of RPS15A rescued proliferation of S15A-eIF3KO cells (Fig 7F), indicating that failure to augment RPS15A levels is the primary reason for the lack of growth stimulation of S15A-eIF3KO cells by depletion of eIF3k. In summary, these data suggest that physical interaction of eIF3 with the 5'-UTR of RPS15A imparts critical control on RPS15A mRNA translation and tumor cell growth.

**Depletion of eIF3k confers stress resistance dependent on the eIF3-binding site in RPS15A mRNA**

Deletion of eIF3k and its binding partner eIF3l was previously shown to confer resistance to tunicamycin-induced endoplasmic

**Figure 7. Effect of eIF3k S15A-eIF3KO cells.**

- A Parental eIF3k-mAID cells or S15A-eIF3KO cells (clones #45 and #361) were maintained in media with DMSO or IAA, and cell numbers were determined at various time points. Data represent means  $\pm$  SD (too small to be visible),  $n = 3$ . All  $P$ -values (two-stage step-up method of Benjamini, Krieger, and Yekutieli) were  $> 0.45$  except at the single time point where indicated otherwise.
- B  $1 \times 10^6$  S15A-eIF3KO (clone #361) cells were injected into nude mice. When tumors reached a diameter of  $\sim 4$  mm, mice were treated with vehicle or 500 mg/kg IAA, and tumor growth was measured for 2 weeks. Graphs represent means  $\pm$  SD,  $n = 5-7$ . Numbers indicate  $P$ -values (two-stage step-up method of Benjamini, Krieger, and Yekutieli).
- C Lysate of S15A-eIF3KO cells (clones #45 and #361) were separated by sucrose density gradient centrifugation. Total ribosome content was determined by integrating and summing the monosomal and polysomal peak areas. Error bars represent means  $\pm$  SD,  $n = 3$  (see Fig EV5B). Numbers indicate  $P$ -values (unpaired Student's  $t$ -test).
- D Total ribosome occupancy of the indicated mRNAs in S15A-eIF3KO (clone #361) cells exposed to DMSO or IAA for 12 h was determined by RT-qPCR of RNA across a sucrose density gradient (see Materials and Methods). Bars represent means  $\pm$  SD,  $n = 3$ ; numbers indicate  $P$ -values (unpaired Student's  $t$ -test). Triplicate RT-qPCR data across the sucrose gradient are shown below the bar graphs.
- E RNA immunoprecipitation. eIF3k-mAID and S15A-eIF3KO (clone #361) cells were exposed to DMSO or IAA for 12 h. Cell lysates were employed in immunoprecipitation with eIF3c antibodies and co-precipitated mRNAs were quantified by qPCR. Bars represent means  $\pm$  SD,  $n = 4$ ; numbers indicate  $P$ -values (unpaired Student's  $t$ -test).
- F Equal numbers of S15A-eIF3KO (clone #361) cells stably expressing ectopic RPS15A (pCDH-RPS15A) or empty vector (pCDH) were plated and counted over a period of 6 days. Graphs represent means  $\pm$  SD,  $n = 3$ . Asterisks denote: \* $P < 0.005$ , \*\* $P < 0.00005$ , \*\*\* $P < 0.000005$  (two-stage step-up method of Benjamini, Krieger, and Yekutieli).

Data information:  $n$  = number of biological replicates.

Source data are available online for this figure.

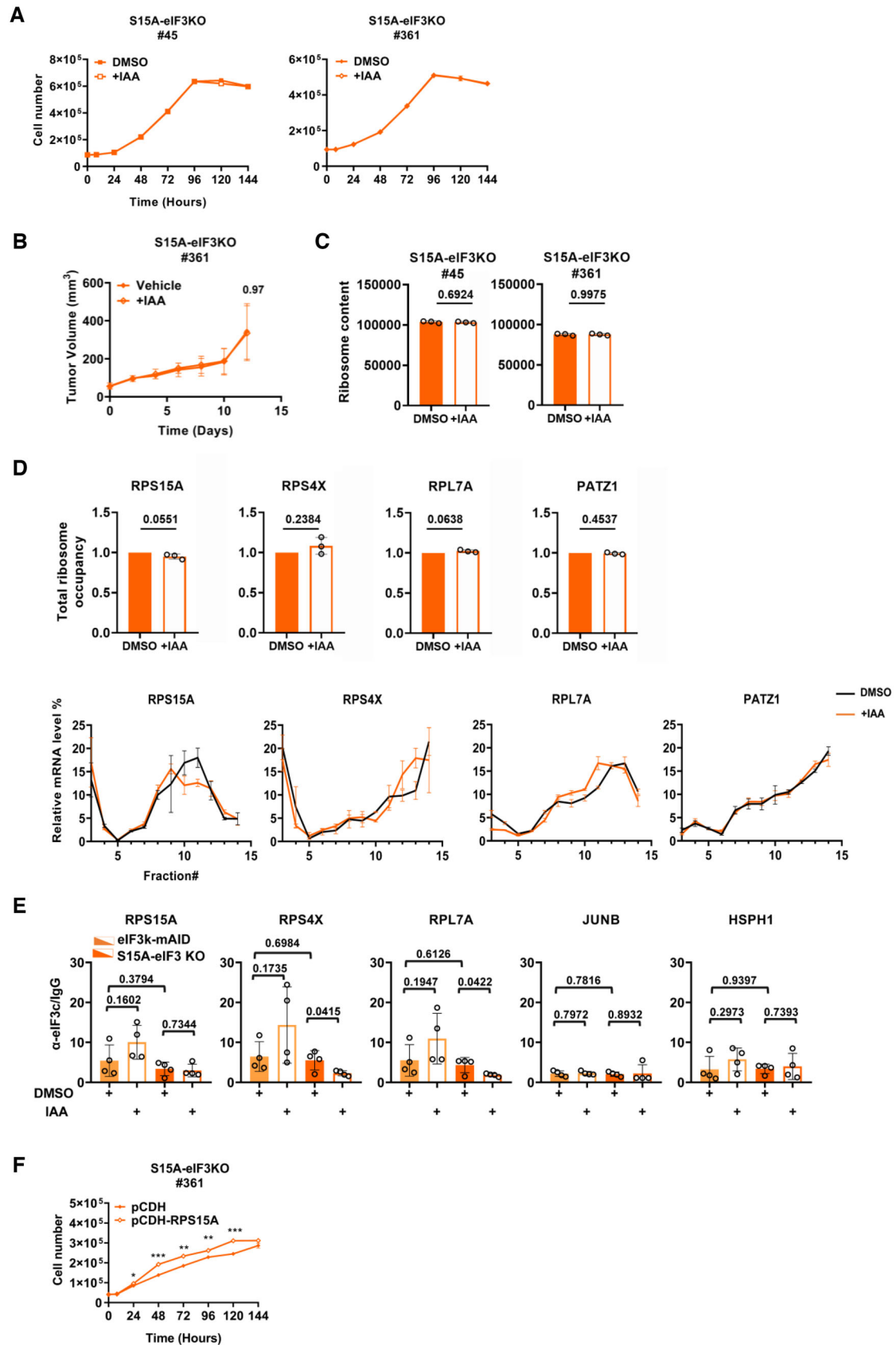
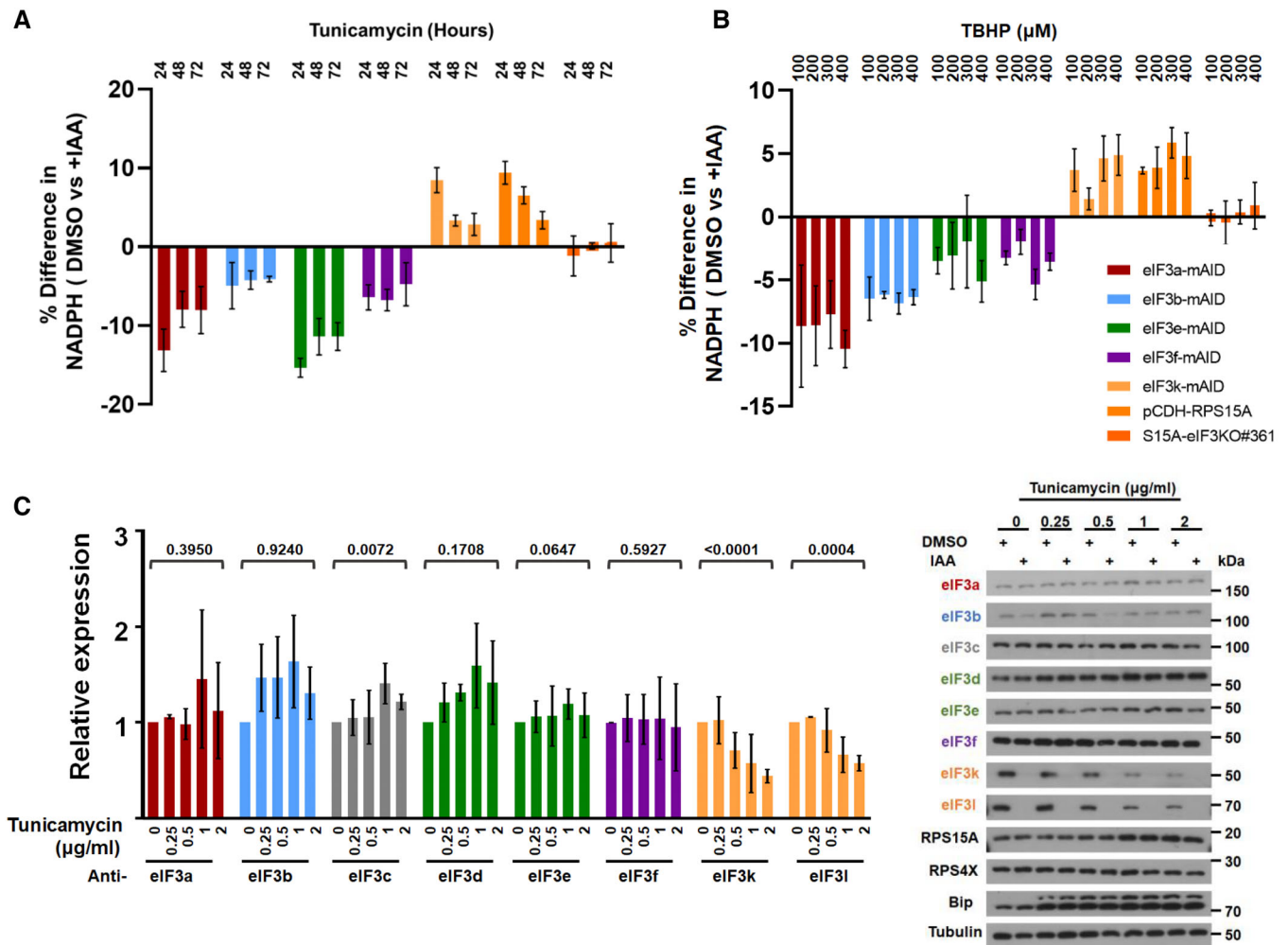


Figure 7.



**Figure 8. Effect of eIF3k on stress sensitivity.**

A The indicated eIF3-mAID cell lines were treated with DMSO or IAA for 12 h, followed by exposure to 2  $\mu\text{g/ml}$  tunicamycin for up to 72 h. Metabolic activity (i.e., NAD(P)H) as a proxy of cell viability was determined by CCK8 assay. Graphs represent the percentage of change in cell viability upon downregulating eIF3 subunits with IAA. Data are means  $\pm$  SD,  $n = 3$ .

B Same experiment as in (A) but cells were exposed to increasing concentrations of the oxidative stress inducer tert-butyl hydroperoxide (TBHP) for 2 h.

C The indicated eIF3-mAID cell lines were treated with DMSO or IAA for 12 h, followed by exposure to 2  $\mu\text{g/ml}$  tunicamycin for 24 h. The expression of individual eIF3 subunits, ribosomal proteins, and the ER stress marker BIP was assessed by immunoblotting. Tubulin is shown for reference. The data from triplicate experiments were quantified and to avoid overcrowding of the graph data obtained from IAA-treated cells were not plotted. Bars represent means  $\pm$  SD,  $n = 3$  (see Appendix Fig S7). Numbers indicate  $P$ -values (unpaired Student's  $t$ -test).

Data information:  $n =$  number of biological replicates.

Source data are available online for this figure.

reticulum (ER) stress in *C. elegans*, although no mechanistic explanation was provided (Cattie et al, 2016). Testing eIF3-mAID cell lines for sensitivity to 2  $\mu\text{g/ml}$  tunicamycin, we found that depletion of eIF3k conferred resistance, whereas cell lines depleted of any of the other eIF3 subunits were sensitive in the CCK-8 assay (Fig 8A, Appendix Fig S7A). eIF3k-mAID cells ectopically expressing RPS15A showed the same resistance as cells depleted of eIF3k, whereas eIF3k depletion did not affect the sensitivity of S15A-eIF3KO cells (Fig 8A, Appendix Fig S7A). Similar behaviors of the various cell lines were observed for oxidative stress induced by tert-butyl hydroperoxide (Fig 8B, Appendix Fig S7B). Taken together, these results

link eIF3k-dependent stress resistance to its role in controlling RPS15A mRNA translation.

Finally, we determined the effect of tunicamycin on the levels of individual eIF3 subunits. Whereas 2  $\mu\text{g/ml}$  tunicamycin for 24 h did not substantially affect the levels of eIF3a, b, c, d, e, and f, eIF3k and eIF3l were selectively downregulated by the treatment (Fig 8C, Appendix Fig S7C). Whereas the underlying mechanisms remain to be established, this response provides a facile mode for creating a cellular eIF3 complex devoid of the eIF3k-l module that could boost cell fitness and tumor growth through RPS15A-dependent increases in ribosome content.

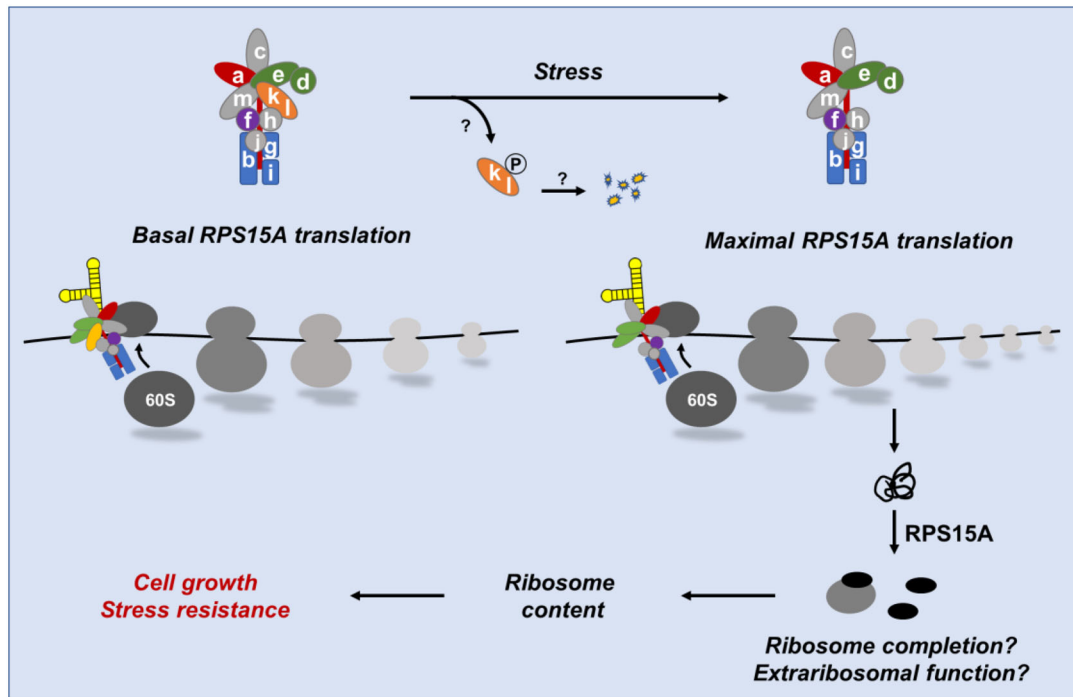


**Figure 9. Model of the dual role of eIF3k in the translation of *RPS15A* mRNA.**

When the eIF3-binding site in the 5'-UTR is occupied by holo-eIF3 containing the eIF3k-l module, *RPS15A* mRNA is translated efficiently at basal rate. When the eIF3k-l module is missing (or functionally inactivated, perhaps degraded in response to stress conditions), the remaining eIF3 complex boosts maximal translation of *RPS15A* mRNA through the eIF3-binding site. The extra *RPS15A* then boosts ribosome content, translation, and growth, for example by completing substoichiometric ribosomes.

## Discussion

### Modular architecture of eIF3 and mRNA selectivity

Our quantitative data on eIF3 complex formation and mRNA translation in cells acutely depleted of eIF3 subunits reinforce the model that holo-eIF3 consists of functionally distinct modules with distinct mRNA selectivity (Zhou *et al*, 2005; Shah *et al*, 2016; Lin *et al*, 2020). Our data are consistent with previous studies relying on knockdown of eIF3 subunits for 72 h (Wagner *et al*, 2014, 2016; Lin *et al*, 2020), but due to the acute depletion afforded by the mAID system, we can assess the effects of eIF3 subunit depletion on holo-eIF3 and mRNA translation largely independent of compensatory effects in response to long-term subunit depletion.

Consistent with its role as a nucleation core of holo-eIF3 formation (Smith *et al*, 2016; Wagner *et al*, 2016), eIF3a was found to be a global regulator of mRNA translation affecting upwards of 5,000 mRNAs in HCT116 cells. The impact of eIF3a is so pervasive that no functional categories were enriched in its set of target mRNAs. Since depletion of eIF3a leads to disassembly of the octameric core complex, it is likely that it abolishes all functions of holo-eIF3 in mRNA translation.

eIF3e affects a far more restricted set of mRNAs, many encoding proteins engaged in mitochondrial and membrane-associated functions. This confirmed our previous findings in fission yeast and human MCF10A cells where eIF3e—likely in complex with eIF3d—functions to promote early translation elongation of mRNAs

encoding membrane-associated proteins (Shah *et al*, 2016; Lin *et al*, 2020). Short-term depletion of eIF3f had a similar effect on holo-eIF3 as depletion of eIF3e and regulated an overlapping set of mRNAs, although its effects on mRNA translation and cell proliferation were less pronounced. This is surprising considering that eIF3f but not eIF3e is essential for viability in *S. pombe* (Zhou *et al*, 2005). Regardless, eIF3f target mRNAs enriched similar mitochondrial and membrane-associated functional categories as the eIF3e dataset, although it is presently unclear whether eIF3f also affects early translation elongation. Our data from HCT116 cells do not support previous conclusions that eIF3f is an inhibitor of global translation (Shi *et al*, 2006); only 17 mRNAs were increased in the polysomal fraction upon depletion of eIF3f (Fig EV3D).

Surprisingly, short-term downregulation of eIF3b by ~73% did not affect mRNA translation despite beginning depletion of the eIF3b-g-i subcomplex. Even at strongly reduced eIF3b levels, cells maintained amounts of holo-eIF3 that are ostensibly sufficient for global mRNA translation (Fig 1C). Nevertheless, as shown by pSILAC proteomics, protein synthesis was reduced in cells depleted of eIF3b for 12 h. This reduction correlated with decreased levels of mRNAs encoding amino acid transporters and tRNA synthetases (Appendix Fig S3C and D), pointing to a possible moonlighting function of eIF3b in mRNA transcription or stability control that may be more sensitive to acute changes in eIF3b levels than its function in translation. Consistent with this possibility, changes at the level of total mRNA are most abundant in eIF3b-depleted cells compared with all other eIF3-mAID cell lines (Fig EV3D) and a fraction of



eIF3b is known to localize to the cell nucleus (<https://www.proteinatlas.org/ENSG00000106263-EIF3B/subcellular#human>).

Despite quantitative and qualitative differences in mRNA selectivity, all tested eIF3 subunits except eIF3k were required for cell and tumor growth. This is consistent with cell autonomous pro-oncogenic functions of these eIF3 subunits and renders studies suggesting tumor suppressor functions of eIF3e and eIF3f difficult to reconcile (Marchione *et al*, 2013; Sesen *et al*, 2017). It is noteworthy in this context that eIF3f is essential in fission yeast (Zhou *et al*, 2005) and eIF3f and eIF3e homozygous knockout mice are early embryonic lethal (Sadato *et al*, 2018; Docquier *et al*, 2019; Lin *et al*, 2020). It is thus unclear what tumor cells stand to gain from reducing the levels of these essential growth-promoting factors.

### Dual function of eIF3 in the regulation of *RPS15A* mRNA translation: possible role of eIF3k as a regulator of ribosome reserve capacity

eIF3k was found to be unique in that its depletion promoted cell and tumor growth, effects presumably mediated by the eIF3k-l module. This unusual gain of fitness was not attributable to increased sensitivity to mitogenic signaling but rather to an increase in total ribosome content and global translation. The observed inverse relationships between eIF3k levels with ribosome content and global translation were recapitulated in the RFM model of mRNA translation, thus underpinning our experimental observations by computational modeling.

*RPS15A* is known to bind eIF3 in its 5'-UTR (Lee *et al*, 2015; Meyer *et al*, 2015), and deleting this binding site had two effects: (i) It reduced cell proliferation and caused a ~50% decrease in *RPS15A* protein. (ii) It prevented the increase in ribosome content and cell and tumor growth induced by depletion of eIF3k. Thus, the eIF3-binding site has a dual function in controlling *RPS15A*: (i) It positively regulates the basal translation of *RPS15A* mRNA, and (ii) it negatively regulates the maximal rate of *RPS15A* mRNA translation via eIF3k (Fig 9). A repressive effect of eIF3 via 5'-UTR binding has previously been described for the mRNA encoding ferritin light chain (Pulos-Holmes *et al*, 2019), although the repression was not attributed to a distinct subunit. eIF3k-mediated repression of *RPS15A* translation thus represents an example of subunit-selective translational repression by eIF3 through an element in the 5'-UTR. Dual positive and negative functions of nucleic acid binding motifs depending on the subunit composition or posttranslational modification of binding protein complexes are well established in transcriptional regulation (Henley & Dick, 2012). In conclusion, through

eIF3k, eIF3 functions as a rheostat to keep *RPS15A* mRNA translation within relatively narrow boundaries.

Whereas ectopic expression of several RPs induces nucleolar stress and p53-dependent growth arrest (Lohrum *et al*, 2003; Zhang *et al*, 2003; Jin *et al*, 2004), ectopic *RPS15A* increased ribosome content and augmented cell and tumor growth. We envision at least two possibilities how *RPS15A* might bring about these dominant effects: (i) *RPS15A* may increase ribosome content through an unknown extra-ribosomal function (Wool, 1996) that broadly promotes ribosome biogenesis. (ii) *RPS15A* may mobilize reserve ribosome capacity, possibly by completing a pool of substoichiometric ribosomes known to exist in *S. cerevisiae* (Yu *et al*, 2020). Similarly, completion of ribosome subunit stoichiometry by boosting the expression of substoichiometric ribosomal proteins was linked to increased cell growth (Slavov *et al*, 2015) and neuronal mRNA translation (Fusco *et al*, 2021).

What might be the physiological role of the proposed function of eIF3k as a rheostat for keeping *RPS15A* mRNA translation within relatively narrow limits? The general picture emerging from studies in microbes (Mori *et al*, 2017; Korem Kohanim *et al*, 2018) and mammalian systems (Slavov *et al*, 2015) is that reserve ribosome capacity endows cells with the ability to respond quickly to changes in environment. For example, ribosome capacity can become limiting under environmental stress conditions when cells are swamped with stress-induced transcripts that need to be turned into new proteins quickly (Lee *et al*, 2011). Our data introduce eIF3k as a new regulator of ribosome capacity at the level of translation. A possible model is that stress signaling triggers the loss or functional inactivation of eIF3k and eIF3l such that the residual eIF3 complex lacking these subunits maximally stimulates *RPS15A* translation (Fig 9). Consistent with this model is the observation that loss-of-function mutations in eIF3k and eIF3l lead to enhanced resistance of *C. elegans* to endoplasmic reticulum stress induced by tunicamycin (Cattie *et al*, 2016), a phenotype we reproduced and extended to oxidative stress in HCT116 cells (Fig 8A and B).

Within the tumor microenvironment, cancer cells are well known to be exposed to rapid fluctuations in nutrient, pH, and redox conditions (Luo *et al*, 2009). In light of our discoveries, the downregulation of eIF3k we identified in human colon and renal cancers may enable tumor cells to tap into ribosome reserves to maximize stress resilience without a substantial cost on growth. If so, this stress mitigation pathway may present an attractive target for interventions geared toward disabling eIF3-boosted ribosome capacity.

## Materials and Methods

### Reagents and Tools table

Reagent/Resource	Reference or Source	Identifier or Catalog Number
<b>Experimental Models</b>		
HCT116 CMV-OsTIR1	Riken Bioresource Research Center of Japan	RCB4662, RRID: CVCL_RJ11
Mouse: BALB/c male nude mice	Xiamen University Laboratory Animal Center	N/A
<b>Recombinant DNA</b>		
<i>RPS15A</i> sgRNA-1 lentiCRISPR v2 plasmid	This manuscript	Addgene submission pending

Reagents and Tools table (continued)

Reagent/Resource	Reference or Source	Identifier or Catalog Number
RPS15A sgRNA-2 lentiCRISPR v2 plasmid	This manuscript	Addgene submission pending
RPS15A sgRNA-4 lentiCRISPR v2-Blast plasmid	This manuscript	Addgene submission pending
RPS15A sgRNA-5 lentiCRISPR v2-Blast plasmid	This manuscript	Addgene submission pending
RPS4X sgRNA-1 lentiCRISPR v2 plasmid	This manuscript	Addgene submission pending
RPS4X sgRNA-2 lentiCRISPR v2 plasmid	This manuscript	Addgene submission pending
RPS4X sgRNA-3 lentiCRISPR v2-Blast plasmid	This manuscript	Addgene submission pending
RPS4X sgRNA-4 lentiCRISPR v2-Blast plasmid	This manuscript	Addgene submission pending
eIF3a- pMK289 (mAID-mClover-NeoR) plasmid	This manuscript	Addgene submission pending
eIF3a- pMK293 (mAID-mCherry2-Hygro) plasmid	This manuscript	Addgene submission pending
eIF3b- pMK289 (mAID-mClover-NeoR) plasmid	This manuscript	Addgene submission pending
eIF3b- pMK293 (mAID-mCherry2-Hygro) plasmid	This manuscript	Addgene submission pending
eIF3e- pMK289 (mAID-mClover-NeoR) plasmid	This manuscript	Addgene submission pending
eIF3e- pMK293 (mAID-mCherry2-Hygro) plasmid	This manuscript	Addgene submission pending
eIF3f- pMK289 (mAID-mClover-NeoR) plasmid	This manuscript	Addgene submission pending
eIF3f- pMK293 (mAID-mCherry2-Hygro) plasmid	This manuscript	Addgene submission pending
eIF3k- pMK289 (mAID-mClover-NeoR) plasmid	This manuscript	Addgene submission pending
eIF3k- pMK293 (mAID-mCherry2-Hygro) plasmid	This manuscript	Addgene submission pending
pCDH-CMV-RPS15A-3xHA plasmid	This manuscript	Addgene submission pending
pCDH-CMV-RPS4X-3xHA plasmid	This manuscript	Addgene submission pending
Px459VQR	Addgene	Cat # 101715
lentiCRISPR v2-Blast plasmid	Addgene	Cat # 83480
lentiCRISPR v2 plasmid	Addgene	Cat # 52961
pMK289 (mAID-mClover-NeoR)	Addgene	Cat # pMK289
pMK293 (mAID-mCherry2-Hygro)	Addgene	Cat # pMK293
pMDLg/pRRE	Addgene	Cat # 12251
pRSV-Rev	Addgene	Cat # 12253
pVSV-G	Addgene	Cat # 138479
pMD2.G	Addgene	Cat # 12259
psPAX2	Addgene	Cat # 12260
pCDH-CMV-MCS-EF1-puro-3xFlag-3xHA	generously provided by L. Wen (Xiamen University)	N/A
<b>Antibodies</b>		
Goat Anti-Rabbit IgG (WB 1:5,000)	Thermo Fisher	Cat # 31460; RRID: AB_228341
Goat anti-Mouse IgG (WB 1:5,000)	Thermo Fisher	Cat # 31430; RRID: AB_228307
Normal Rabbit IgG	Cell Signaling Technology	Cat # 2729; RRID: AB_1031062
Mouse Monoclonal anti-β-Actin (WB 1:2,000)	SIGMA-ALDRICH	Cat # A5441; RRID: AB_476744
Mouse Polyclonal anti-α-Tubulin (WB 1:2,000)	Santa Cruz Biotechnology	Cat # sc-398103; RRID: AB_476744
Mouse Monoclonal anti-mini AID-tag (WB 1:2,000)	MBL	Cat # M214-3; RRID: AB_2890014
Mouse Monoclonal Anti-HA tag (WB 1:2,000)	Abclonal	Cat # AE008; RRID: AB_2770404
Rabbit Polyclonal Anti-eIF3a (WB 1:2,000)	Novus	Cat # NBP1-18891; RRID: AB_1625664
Rabbit Polyclonal Anti- eIF3b (WB 1:2,000)	Bethyl	Cat # A301-761A; RRID: AB_1210995
Rabbit Polyclonal Anti- eIF3c (WB 1:2,000)	Bethyl	Cat # A300-377A; RRID: AB_2096755

**Reagents and Tools table** (continued)

Reagent/Resource	Reference or Source	Identifier or Catalog Number
Rabbit Polyclonal Anti- eIF3d (WB 1:2,000)	Bethyl	Cat # A301-758A; RRID: AB_1210970
Rabbit Polyclonal Anti- eIF3e (WB 1:2,000)	Bethyl	Cat # A302-985A; RRID: AB_10749034
Rabbit Polyclonal Anti- eIF3f (WB 1:2,000)	Bethyl	Cat # A303-005A; RRID: AB_10748371
Rabbit Polyclonal Anti- eIF3g (WB 1:2,000)	Bethyl	Cat # A301-757A; RRID: AB_1210991
Rabbit Polyclonal Anti- eIF3i (WB 1:2,000)	Abcam	Cat # ab128629; RRID: AB_2863386
Rabbit Polyclonal Anti- eIF3k (WB 1:2,000)	Novus	Cat # NB100-93304; RRID: AB_1236913
Rabbit Polyclonal Anti- eIF3l (WB 1:2,000)	GeneTex	Cat # GTX120119; RRID: AB_11169154
Rabbit Polyclonal Anti- RPL7 (WB 1:2,000)	Abcam	Cat # ab72550; RRID: AB_1270391
Rabbit Polyclonal Anti- RPS19 (WB 1:2,000)	Bethyl	Cat # A304-002A; RRID: AB_2620351
Rabbit Polyclonal Anti- RPS15A (WB 1:2,000)	Abclonal	Cat # A10241; RRID: AB_2757767
Rabbit Polyclonal Anti- RPS4X (WB 1:2,000)	Abclonal	Cat # A6730; RRID: AB_2767314
Rabbit Monoclonal Anti- mTOR (7C10) (WB 1:2,000)	Cell Signaling Technology	Cat # 2983; RRID: AB_2105622
Rabbit Monoclonal Anti- Phospho-mTOR (Ser2448) (D9C2) (WB 1:2,000)	Cell Signaling Technology	Cat # 5536; RRID: AB_10691552
Rabbit Polyclonal Anti- p70 S6 Kinase (49D7) (WB 1:2,000)	Cell Signaling Technology	Cat # 2708; RRID: AB_390722
Rabbit Polyclonal Anti- Phospho-p70 S6 Kinase (Thr389) (WB 1:2,000)	Cell Signaling Technology	Cat # 9234; RRID: AB_2269803
Rabbit Monoclonal Anti- ERK1/2 (WB 1:2,000)	Abclonal	Cat # A4782; RRID: AB_2863347
Rabbit Monoclonal Anti- Phospho-ERK1/2 (Thr389) (WB 1:2,000)	Abclonal	Cat # AP0974; RRID: AB_2863871
Rabbit Monoclonal Anti- Bip /GRP78 (WB 1:2,000)	Abclonal	Cat # A4908; RRID: AB_2863386
<b>Oligonucleotides and sequence-based reagents</b>		
PCR primers or RT-qPCR primer	This study	Table EV1
<b>Chemicals, enzymes and other reagents</b>		
DNase I	NEB	Cat # M0303
Recombinant RNasin	Promega	Cat # N2511
Pierce protease inhibitor cocktail	MedChem Express	Cat # HY-K0011
Trypsin Gold, MS Grade	Promega	Cat # V5280
Sure Beads™ Protein A Magnetic beads	BIO-RAD	Cat # 1614813
Cycloheximide	Cell Signaling Technology	Cat # 2112
Rapamycin	MCE	Cat # 53123-88-9
Tunicamycin	BBI	Cat # A611129
Tert-butyl hydroperoxide	MACKLIN	Cat # 75-91-2
BsmBI	New England Biolabs	Cat # R0580S
BbsI	New England Biolabs	Cat # R0539S
XbaI	New England Biolabs	Cat # R0145S
XhoI	New England Biolabs	Cat # R0146S
BamHI	New England Biolabs	Cat # R3136S
T4 Polynucleotide Kinase	New England Biolabs	Cat # M0201S
T4 DNA Ligase	New England Biolabs	Cat # M0202S
CIP	New England Biolabs	Cat # M0290S
<b>Software</b>		
GraphPad Prism 8	GraphPad Software, Inc	<a href="https://www.graphpad.com/scientific-software/prism/">https://www.graphpad.com/scientific-software/prism/</a>

Reagents and Tools table (continued)

Reagent/Resource	Reference or Source	Identifier or Catalog Number
UV gradient profiling software	BIOCOMP	Version 7.73
FlowJo 7.6	FlowJo LLC	<a href="https://www.flowjo.com/solutions/flowjo/downloads">https://www.flowjo.com/solutions/flowjo/downloads</a>
ZEN software	ZEISS Microscopy	<a href="https://portal.zeiss.com/download-center/software/mic">https://portal.zeiss.com/download-center/software/mic</a>
ImageJ	Schneider <i>et al</i> (2012)	<a href="https://imagej.en.softonic.com/">https://imagej.en.softonic.com/</a>
Java Treeview	Java Treeview--extensible visualization of microarray data – PubMed (nih.gov)	<a href="https://sourceforge.net/projects/jtreeview/files/">https://sourceforge.net/projects/jtreeview/files/</a>
Metascape	Zhou <i>et al</i> (2019)	Metascape
Thermo Proteome Discoverer (PD 2.1.1.2)	Thermo	Proteome Discoverer Software   Thermo Fisher Scientific – CN
CFU Scope	Medixgraph Inc.	<a href="http://medixgraph.com/cfscope">http://medixgraph.com/cfscope</a>
R Studio	N/A	RStudio   Open source & professional software for data science teams – RStudio
<b>Other</b>		
Thermo Scientific™ Multiskan™ FC	Thermo Scientific	Cat # 1410101
UV detector	BIO-RAD	ECONO UV MONITOR
Piston Gradient Fractionator	BIOCOMP	Cat # B152-002
Gradient master	BIOCOMP	#108
ChemiDoc™ imaging system	BIO-RAD	Cat # 733BR2378
ATTUNE NXT Flow Cytometer	Thermo Scientific	Cat # A29001
Caliper IVIS Lumina II instrument	Caliper	IVIS Lumina II
Q5® Site-Directed Mutagenesis Kit	New England Biolabs	Cat # E0554
Monarch® RNA Cleanup Columns	New England Biolabs	Cat # T2047L
SanPrep Column DNA Gel Extraction Kit	Sangon Biotech	Cat # B518131
EndoFree Mini Plasmid Kit II	TIANGEN	Cat # DP118-02
TransScript All-in-One First-Strand cDNA Synthesis SuperMix	Trans	Cat # AT341-01
TransStart Top Green qPCR SuperMix	Trans	Cat # AQ131-01
TRIzol LS reagent	Thermo Fisher	Cat # 10296010
7.5% PAGE Gel Fast Preparation Kit	EpiZyme	Cat # PG111
10% PAGE Gel Fast Preparation Kit	EpiZyme	Cat # PG112
12.5% PAGE Gel Fast Preparation Kit	EpiZyme	Cat # PG113
PAGE Sample Prep Kit	Thermo Fisher	Cat # BN2008
Native PAGE Gel	Thermo Fisher	Cat # BN1004BOX
BCA Protein Assay Kit	TIANGEN	Cat # R6628

## Methods and Protocols

### Cell lines

The male HCT116 cell line expressing OstTIR1 (Natsume *et al*, 2016) was obtained from the Riken Bioresource Research Center of Japan and was cultured in McCoy's 5A medium (Thermo Fisher Scientific) supplemented with 10% FBS (Gibco), 2 mM L-glutamine, 100 U/ml penicillin, and 100 mg/ml streptomycin at 37°C and 5% CO<sub>2</sub>. Cells were periodically determined to be free of mycoplasma.

### Mice

BALB/c male nude mice (4–6 weeks of age) were used for subcutaneous xenografts. Mice were housed under pathogen-free conditions

and maintained on a 12-h light/12-h dark cycle with food and water supplied *ad libitum*.

### Generation of cell lines

To generate cell lines in which both alleles of eIF3 subunits were tagged with mAID-mClover and mAID-mCherry, donor plasmids were constructed according to (Natsume *et al*, 2016). Homology arm fragments for eIF3a, b, e, f, and k containing a central BamHI site were obtained by gene synthesis and cloned into a donor plasmid. In a second step, the respective mAID-mClover and mAID-mCherry cassettes containing a selection marker were cloned at the BamHI site between the homology arms. Homology arms were designed to mutate the recognition sequence after integration at the



target locus to prevent recutting. HCT116-OsTIR1 cells were grown in 6-well plates before 800 ng Cas9 plasmid and 600 ng mAID donor plasmids (Reagent Table) were co-transfected using 8  $\mu$ l Lipofectamine 2000. 48 h after transfection, cells were replated on 10 cm dishes and selected with 700  $\mu$ g/ml G418 and 100  $\mu$ g/ml HygroGold. After 12 days, colonies were picked and verified by PCR and Sanger sequencing and by immunoblotting. The list of primers for the various truncation and point mutants is summarized in the Reagent Table. To induce the degradation of mAID-fused proteins, 500  $\mu$ M indole-3-acetic acid (IAA) was added to the culture medium.

To generate eIF3k-mAID cells in which the eIF3-binding sites in the 5'-UTRs of RPS15A and RPS4X were deleted, targeting plasmids were constructed according to the protocol by Ran et al (2013). Cas9 cutting sites 3' and 5' of the region to be deleted were identified using a web tool (<http://crispor.tefor.net/>, (Concordet & Haeussler, 2018)). Pairs of corresponding sgRNAs were individually cloned into either BsmBI-digested lentiCRISPR v2-Blast or lentiCRISPR v2-Puro. To produce virus, HEK293T cells at ~50% confluence were transfected in 35 mm dishes with 0.5  $\mu$ g pMD2.G and 0.75  $\mu$ g psPAX2 packaging vectors and 1  $\mu$ g of the lentiCRISPR v2 plasmid with 5  $\mu$ l Lipofectamine 2000 in optiMEM. The medium was exchanged for DMEM high glucose medium with 10% FBS after 6 h. Virus supernatant was collected after 48 h, passed through a 0.45  $\mu$ m filter, and stored at -80°C. 30% confluent eIF3k-mAID cells were infected by pairs of sgRNA virus in 35 mm dishes with 8  $\mu$ g/ml polybrene. After 24 h, the medium was exchanged for McCoy's 5A, and cells were selected for 1 week in puromycin (4  $\mu$ g/ml) and blasticidin (30  $\mu$ g/ml). A small fraction of the infected cells was collected to determine the efficiency of CRISPR editing. Different combinations of guide RNAs showed different efficiency. Cells infected with the most efficient pair of guide RNA viruses were expanded, and single colonies were picked and confirmed by genomic PCR and Sanger sequencing. The list of primers for various truncation is summarized in Table EV1.

For stable overexpression of RPS15A and RPS4X in eIF3k-mAID cells, a recombinant lentivirus was constructed by inserting the PCR-amplified cDNA sequence into XhoI and XbaI sites of pCDH-CMV-MCS-EF1-puro-3xFlag-3xHA (generously provided by L. Wen). 293T cells were transfected with the packaging plasmids pMDLg/pRRE, pVSV-G, and pRSV-Rev at a ratio of 0.5: 0.3: 0.2  $\mu$ g and 1  $\mu$ g pCDH-CMV-RPS15A-3xHA or pCDH-CMV-RPS4X-3xHA plasmids. Virus collection and infection was as described previously. After infection, cells were selected with puromycin (4  $\mu$ g/ml) for 7 days and lysate of polyclonal cultures was tested for RPS15A expression by immunoblotting.

#### Proliferation/viability assays

Commonly used tetrazolium dye reduction assays measuring NAD (P)H levels (MTT and CCK-8) were employed as surrogate measures of cell proliferation/viability.  $8 \times 10^3$  cells per well were seeded into 96 well plates. Cells were incubated with 10  $\mu$ l of CCK8 reagent and incubated at 37°C until color development. Absorbance measurements were performed at 450 nm using a microplate reader (Thermo Scientific™ Multiskan™ FC). For MTT assays, 20  $\mu$ l of MTT reagent at 5 mg/ml was added into each well for a final concentration of 0.5% and incubated for 4 h at 37°C. The medium was removed, and 100  $\mu$ l 100% DMSO was added to each well followed by vigorous

mixing. After incubation at room temperature for 10 min, samples were mixed, and absorbance was measured at 540 nm in a microplate reader (Thermo Scientific™ Multiskan™ FC).

#### Colony formation assay

$1 \times 10^3$  cells were plated on 100 mm culture dishes in three replicates and cultured for 2 weeks. After removal of media and washing in PBS, 10 ml methanol was added, and cells were fixed for 30 min. Upon removal of methanol, cells were stained with crystal violet in 20% methanol in PBS for 30 min, rinsed with water, and dried. Colony numbers were determined with CFU Scope.

#### Cell cycle analysis by flow cytometry

Cells were collected by trypsinization and washed with cold PBS and then fixed in cold 70% ethanol at 4°C for a minimum of 2 h. Fixed cells were treated with 100  $\mu$ g/ml RNase and stained with 50  $\mu$ g/ml propidium iodide in PBS for 15–30 min in the dark. Samples were run on an ATTUNE NXT Flow Cytometer (Thermo Fisher Scientific), and data were analyzed with FlowJo software.

#### Xenografts studies

Animal experiments were performed in accordance with the Guiding Principles in the Care and Use of Animals (China) and were approved by the Laboratory Animal Ethics Committee of Xiamen University.  $1 \times 10^6$  cells in a volume of 100  $\mu$ l were inoculated subcutaneously into nude mice. After tumor reached a diameter of ~4 mm (~50 mm<sup>3</sup>), IAA (500 mg/kg body weight in corn oil) or an equal amount of corn oil vehicle was administered by oral gavage daily for 2 weeks. Tumor sizes were monitored every 2 days by measurement with a caliper and body weights were recorded. Tumor volumes were calculated according to the formula: volume = width<sup>2</sup> × length/2. Mice were sacrificed after 2 weeks, and tumors were excised for analysis. Tumor imaging was done on a Caliper IVIS Lumina II instrument with imaging mode set to Fluorescence, exposure time to 1 min, and excitation and emission filter set to 465 nm and 515–575 nm, respectively.

#### Immunoblotting

For protein extraction, cells were washed twice with cold PBS, scraped off, and lysed in SDS sample buffer (60 mM Tris-HCl, pH 6.8, 5% beta-mercaptoethanol, 2% SDS, 10% glycerol, 0.02% bromophenol blue) followed by heating for 8 min at 95°C. Lysates were separated by SDS-PAGE, and immunoblotting was done as described (Tian et al, 2021). Primary antibodies used in this study are listed in the Reagent Table. Quantification of band intensities was done using ImageJ software.

#### Native PAGE analysis

Cells contained in a 35 mm dish at 70–80% confluence were lysed in 250  $\mu$ l native lysis buffer supplemented with 1% digitonin by pipetting up and down 10 times and incubation on ice for 10 min. Lysates were centrifuged at 20,000 g for 30 min at 4°C. Protein concentration was measured by BCA protein assay and Coomassie blue G-250 was added to a final concentration of 0.25%. Equal amounts of protein (20  $\mu$ g) were resolved on 4–16% Native PAGE gels. After filling the upper buffer chamber (inner) with blue cathode buffer (0.02% Coomassie Blue G, 15 mM bis-tris, 50 mM tricine, pH 7.0) and the lower (outer) buffer chamber with anode

buffer, electrophoresis was performed at 10 mA on ice. Once the dye front had migrated into 1/3 of the gel, the blue cathode buffer was replaced with cathode buffer (15 mM Bis-tris, 50 mM tricine, pH 7.0). The electrophoresis was continued for 90–100 min at 10 mA. Gels were transferred to PVDF membranes followed by immunoblotting as described previously.

#### Sucrose density gradient separation of ribosomes and RT-qPCR

10 min prior to harvest, 100 µg/ml cycloheximide (CHX) was added to cells contained in two 15 cm dishes at approximately 80% confluence. Cells were incubated in 0.5 ml hypotonic buffer (5 mM Tris-HCl, pH 7.5, 2.5 mM MgCl<sub>2</sub>, 1.5 mM KCl and 1 × Pierce™ protease inhibitor cocktail) supplemented with 100 µg/ml CHX, 1 mM DTT, and 100 units of RNase inhibitor on ice for 20 min and vortexed for 15 s. Triton X-100 and sodium deoxycholate were added to a final concentration of 0.5%, and the lysate was vortexed for another 5 s. The cell lysates were centrifuged at 16,500 g, at 4°C for 7 min. Supernatants were collected, and absorbance at 260 nm was measured. 20–30 OD<sub>260</sub> of lysate was gently layered over 10–50% sucrose gradients in buffer (20 mM HEPES-KOH, pH 7.6, 5 mM MgCl<sub>2</sub>, 100 mM KCl, 100 µg/ml CHX, 10 units/ml RNase inhibitor and 1 × Pierce™ protease inhibitor cocktail). Gradients were centrifuged at 220,000 g (Beckman, SW41Ti) for 2 h at 4°C. After centrifugation, 15 fractions (0.74 ml/ fraction) were collected on a BIOCAMP gradient fractionator.

For RT-qPCR, total RNA was isolated from 250 µl of each gradient fraction using TRIzol LS reagent. cDNA was generated from equal amounts of RNA by reverse transcription using the TransScript All-in-One First-Strand cDNA Synthesis SuperMix for qPCR. The relative quantity of specific mRNAs was measured by quantitative polymerase chain reaction (qPCR) using the TransStart Top Green qPCR SuperMix with the Real-Time PCR System. Primers for qPCR are listed in Table EV1. Total ribosome occupancy was calculated according to the method of Darnell *et al* (2011). The percentage of mRNA in each fraction as determined by qPCR was multiplied by the number of ribosomes in that fraction (extrapolated from UV traces based on the linearity of the sucrose density gradient) and summed over the gradient.

#### Pulsed SILAC

Cells were grown in McCoy's 5A media (SILAC standard, 88441) containing light (<sup>12</sup>C, <sup>14</sup>N) lysine and arginine supplemented with 10% dialyzed FBS for 2 weeks. 2 × 10<sup>6</sup> cells were treated with 500 µM IAA or DMSO for 6 h before switching to heavy medium containing (<sup>13</sup>C, <sup>15</sup>N) lysine and arginine supplemented with 500 µM IAA. After another 6 h, cells were scraped in precooled PBS and pelleted. Cell pellets were resuspended in 0.5 ml 8 M urea lysis buffer (8 M urea in 100 mM Tris-HCl, pH 8.0). Following centrifugation at 12,000 g for 15 min at 4°C, supernatants were collected, and protein concentrations were determined by BCA assay. 200 µg protein was loaded onto a Microcon Centrifugal Filters (Millipore, Cat: 42407). Filter-aided sample preparation (FASP) for LC-MS/MS was done as described (Wićniewski *et al*, 2011). The digested peptide mixtures were redissolved in 0.1% formic acid in ultrapure water, and LC-MS/MS was performed as described (Lin *et al*, 2020). Protein identification and quantitation were performed with Thermo Proteome Discoverer (PD 2.1.1.2.) software searching against the UniProt human protein database release 2018\_04. Triplicate

LC-MS/MS datasets were subjected to statistical testing (Benjamini-Hochberg) to identify proteins whose synthesis (Log<sub>2</sub> Heavy IAA/Heavy DMSO) was changed upon depletion of eIF3 subunits at an FDR ≤ 0.1.

#### Quantitative proteomics of eIF3 complexes

eIF3-mAID cell lines were grown in McCoy's 5A media (SILAC standard, 88441) containing light (<sup>12</sup>C, <sup>14</sup>N) lysine and arginine or containing heavy (<sup>13</sup>C) lysine and arginine for 2 weeks. 12 h prior to harvest, 500 µM IAA or vehicle (DMSO) were added. Cells were collected and lysed in IP buffer (20 mM Tris-HCl pH 7.5, 150 mM NaCl, 0.5% Triton X-100 and 1 × Pierce™ protease inhibitor cocktail) through rotation for 15 min at 4°C. Supernatants were collected after centrifugation at 13,000 g for 15 min at 4°C, and protein concentrations were determined by BCA assay. Lysates were split into two equal parts and 2 µg antibodies (anti-eIF3b or anti-eIF3c) were added and incubated by rotating overnight at 4°C. 50 µl Protein A Surebead (BIO-RAD, #1614813) was added to the samples. Following incubation at 4°C for 4 h with constant rotation, beads were washed with 500 µl IP buffer 3 times 10 min each. Following trypsin digestion, corresponding heavy and light samples were mixed at a ratio of 1:1. After desalting, peptide mixtures were redissolved in 0.1% formic acid in ultrapure water, and LC-MS/MS, protein identification and quantitation were performed as described previously.

#### Quantitative proteomics of ribosomal proteins

250 µl of polysomal fractions 11–14 from a sucrose density gradient was concentrated to 20 µl using Amicon® Ultra-4 Centrifugal Filter Units (Millipore, UFC801024). Proteins were prepared by in-gel digestion (Wu *et al*, 2017). After desalting, peptide mixtures were redissolved in 0.1% formic acid in ultrapure water, and LC-MS/MS, protein identification and quantitation were performed as described previously.

#### RNA extraction and RNA sequencing

Total RNA and RNA contained in heavy polysomal fractions were isolated using the Trizol reagent (Life Technology). Library preparation for bulk-sequencing of poly(A)-RNA was done as described previously (Parekh *et al*, 2016). Briefly, barcoded cDNA of each sample was generated with a Maxima RT polymerase (Thermo Fisher) using oligo-dT primer containing barcodes, unique molecular identifiers (UMIs) and an adaptor. 5'-Ends of the cDNAs were extended by a template switch oligo (TSO), and full-length cDNA was amplified with primers binding to the TSO site and the adaptor. NEB UltraII FS kit was used to fragment cDNA. After end repair and A-tailing, a TruSeq adapter was ligated, and 3'-end-fragments were finally amplified using primers with Illumina P5 and P7 overhangs. In comparison with (Parekh *et al*, 2016), the P5 and P7 sites were exchanged to allow sequencing of the cDNA in read1 and barcodes and UMIs in read2 to achieve a better cluster recognition. The library was sequenced on a NextSeq 500 (Illumina) with 57 cycles for the cDNA in read1 and 16 cycles for the barcodes and UMIs in read2. Data were processed using the published Drop-seq pipeline (v1.0) to generate sample- and gene-wise UMI tables (Macosko *et al*, 2015). Reference genome (GRCh38) was used for alignment. Transcript and gene definitions were used according to the GENCODE version 38.

### RNA-seq data analysis

Only genes with at least one raw read in all samples were retained in the analysis. Raw RNA-seq datasets were normalized for sequencing depth by calculating counts per million mapped reads (CPM) using the EdgeR package (version 3.38.0) in R. For polysomal RNA samples, an additional normalization step was performed according to the formula  $CPM \times (P_{IAA} / P_{DMSO})$  with  $P_x$  signifying the area under the curve of the polysomal fraction of the corresponding lysates separated by sucrose gradient centrifugation. This normalization was done to account for the different levels in total polysomes in the DMSO and IAA-treated sample. This was particularly important for those cell lines that showed a strong decrease in polysomes, including eIF3a-mAID, eIF3e-mAID, and eIF3f-mAID; but for consistency, the normalization was performed for all six cell lines. In the subsequent step, edgeR (Robinson *et al*, 2010) was used to identify changed mRNAs. mRNAs were considered changed in either total or polysome RNA-seq if they differed between the DMSO-treated and IAA-treated samples ( $\text{Log}_2 \text{ IAA/DMSO}$ ) with  $\text{FDR} \leq 0.05$ . Translational efficiencies (TEs) were calculated as  $\text{Log}_2 [(\text{polysomal mRNA IAA} / \text{total mRNA IAA}) / (\text{polysomal mRNA DMSO} / \text{total mRNA DMSO})]$  for data with  $\text{cpm} \geq 10$ . Significance was determined with the R-package's  $P$ -adjust function with the  $\text{FDR} \leq 0.2$ .

### RNA immunoprecipitation and qPCR

Cells were cultured to a density of 70–80% in McCoy's 5A in 150 mm dishes and lysed in 800  $\mu\text{l}$  RNA immunoprecipitation (RIP) lysis buffer containing 20 mM Tris-HCl pH 7.5, 130 mM KCl, 10 mM  $\text{MgCl}_2$ , 1 mM EDTA, 0.5% NP-40, 0.5% sodium deoxycholate, 0.5 mM DTT supplemented with  $1 \times$  Pierce protease inhibitor cocktail, 100 U/ml RNase inhibitor, 0.4 U/ml DNase. The lysate was incubated on ice for 15 min. The supernatants were collected after centrifugation at 13,000  $g$  for 15 min at 4°C, and protein concentrations were determined by BCA assay. 3  $\mu\text{g}$  rabbit IgG or anti-eIF3c antibody were attached to 20  $\mu\text{l}$  Protein A Surehead in RIP lysis buffer for 30 min at room temperature. Beads were washed three times in RIP lysis buffer and added to 1.2 mg protein lysate followed by rotation for 4 h at 4°C. Beads were washed four times for 5 min at 4°C with RIP washing buffer containing 0.1% SDS, 1% Triton X-100, 2 mM EDTA, 20 mM Tris-HCl pH 8.0, 500 mM NaCl. Bound RNA was isolated from the washed beads by adding Trizol and quantified by qPCR as described previously.

### Functional pathway analysis

For each given gene list, pathway and process enrichment analysis has been carried out with Metascape ([metascape.org](https://metascape.org); Zhou *et al*, 2019) with the following ontology sources: GO Biological Processes, GO Cellular Components. Those 9,895 human proteins which we detected by LC-MS/MS in all combined datasets were used as the background dataset. Terms with a  $P$ -value  $< 0.01$ , a minimum count of 3, and an enrichment factor  $> 1.5$  (the enrichment factor is the ratio between the observed counts and the counts expected by chance) were collected and grouped into clusters based on their membership similarities. According to the description at [metascape.org](https://metascape.org),  $P$ -values were calculated based on the accumulative hypergeometric distribution, and  $q$ -values were calculated using the Benjamini-Hochberg procedure to account for multiple testing.

### Computational modeling

We created a dynamical model, which consists of a network of a ribosome flow model (RFM) and a pool of free ribosomes (i.e., ribosomes that are not attached to any mRNA molecule) to analyze the effect of the different eIF3 subunits on translation similar to the approach used in (Zarai & Tuller, 2018). The RFM is a deterministic mathematical model that can be used to model and analyze many transport phenomena (Reuveni *et al*, 2011). It is based on a simple exclusion principle of  $n$  compartments (or sites, e.g., a site along the mRNA, gene, microtubule) with  $n$  state variables describing the compartments' particle density and  $n$  dynamical equations describing the flow dynamics between these compartments as a function of time. The flow between consecutive compartments is controlled by  $\lambda_i$  parameters. Specifically,  $\lambda_0$  denotes the initiation rate,  $\lambda_i$ ,  $i \in \{1, \dots, n-1\}$ , denotes the elongation rate from site  $i$  to site  $i+1$ , and  $\lambda_n$  denoted the exit rate. These rates depend on various factors, including the availability of tRNA molecules, amino acids, aminoacyl tRNA synthetase activity and concentration, and local mRNA folding. We denote by  $R$  the steady-state output flow and by  $e_i$ ,  $i = 1, \dots, n$ , the steady-state particle density at site  $i$ . In the context of mRNA translation,  $R$  is the steady-state translation rate (i.e., the steady-state protein production rate), and  $e_i$  is the steady-state ribosomal density at site  $i$ .

As a specific example, we modeled the translation of the gene TP53 (transcript ENST00000269305.9), which contains 393 amino acids. We divided the ORF to nonoverlapping pieces. The first piece includes the first nine codons that are related to various stages of initiation (Tuller & Zur, 2015). The other pieces include 10 nonoverlapping codons each, except for the last one that includes between 5 and 15 codons. We model every piece of the ORF as a RFM site, resulting in 38 sites. We estimated the elongation rates  $\lambda_i$  at each site using ribo-seq data from HEK293 cells for the codon decoding rates (Dana & Tuller, 2015), normalized so that the median elongation rate becomes five codons per second. We note that similar modeling can be performed for any transcript.

Let  $z$  denote the free ribosomal pool,  $v_k$  the eIF3k concentration value, and let

$$g_{v_k} := d_1 + d_2 e^{-v_k},$$

where  $d_1 > 0$  and  $d_2 > 0$  are constant parameters. We model  $z$  as

$$z = z(v_k) := z_0 g_{v_k},$$

where  $z_0$  denotes the free ribosomal pool governed by the dynamics with the RFM (see below), and  $g_{v_k}$  models the effect of  $v_k$  on the free ribosomal pool.

Let  $f(v) := c_1 + c_2(1 - e^{-v})$ , for all  $v \geq 0$ , and for any positive parameter set  $c_1, c_2$ . We use  $f(v)$  to model the effect of each eIF3 a, b, e, and f subunit on the translation initiation rate, where  $v$  denotes the corresponding subunit concentration value. The parameter  $c_1$  and  $c_2$  can generally vary between the a, b, e, and f subunit models; however, for simplicity they are assumed to have the same values for all these models in the analysis.

Let

$$f_v := f(v_a)f(v_b)f(v_e)f(v_f),$$

denote the product of the subunits a, b, e, and f models. Let  $x_i = x_i(t)$  denote the ribosomal density at site  $i$  (in the RFM) at time  $t$ ,  $\dot{x}_i := dx_i/dt$ , and

$$\eta = \tanh(q * z) = \tanh(q * z_0 * g_{v_k}),$$

where  $q > 0$  is a normalization factor, and  $\tanh()$  is the hyperbolic tangent function. The usage of this function is derived from Zarai and Tuller (2018).

The equations of our dynamical model, which consists of a network of a RFM and the free ribosomal pool and is based on (Zarai & Tuller, 2018), are given by

$$\begin{aligned}\dot{x}_1 &= \lambda_0 f_v \eta (1 - x_1) - \lambda_1 x_1 (1 - x_2), \\ \dot{x}_i &= \lambda_{i-1} x_{i-1} (1 - x_i) - \lambda_i x_i (1 - x_{i+1}), \quad i = 2, \dots, n-1, \\ \dot{x}_n &= \lambda_{n-1} x_{n-1} (1 - x_n) - \lambda_n x_n, \\ \dot{z}_0 &= \lambda_n x_n - \lambda_0 f_v \eta (1 - x_1).\end{aligned}$$

This dynamical model admits a unique steady state for a given total number of ribosomes in the network (Raveh et al, 2016). The concentrations of the eIF3a, b, e, and f subunits affect the effective initiation rate by the product  $\lambda_0 f_v$ . eIF3k concentration affects the free ribosomal pool, which in turn affects the effective initiation rate by the product  $\lambda_0 f_v \eta$ . The dynamical model parameter values used in the simulations were tuned based on the experimental findings and the requirement that  $\lambda_0 f_v (0.5) = \frac{3.6}{60} = 0.06$  (Yan et al, 2016), and are given by:  $c_1 = 0.59$ ,  $c_2 = 1.11$ ,  $d_1 = 487.5$ ,  $d_2 = 412.5$ , and  $q = 1.2 * 10^{-5}$ . Given these parameter values, the steady-state free ribosomal pool at 0.5 concentration of each eIF3 subunit is 56,356.

We determined the robustness of the model by changing ribosome step size down to 1 codon per site and by varying eIF3k parameters  $d_1$  and  $d_2$ . The data showed that the qualitative behavior of the free ribosome pool and the translation rate as a function of the concentrations of eIF3 subunits is similar under the different scenarios (Appendix Fig S8). In order to tailor the model to a specific system, additional experimental data will be needed to estimate the exact set of parameters. This can include, for example, ribo-seq experiments that are combined with modulations of the levels of different eIF3 subunit concentrations.

We also modeled the approximative quantitative relationship between eIF3k and the free ribosome pool. Let the free ribosomal pool k-gain (k-gain for short) denote the ratio between the increase of the steady-state free ribosomal pool (measured in percentage) and the corresponding decrease (depletion) of the eIF3k concentration (measured in percentage). For example, a 10% depletion of eIF3k that results in a 4% increase in the steady-state free ribosomal pool yields  $k\text{-gain} = 4/10 = 0.4$ . As depicted in Fig EV4D, k-gain increases with the eIF3k concentration (as expected). At the nominal concentration of 0.5,  $k\text{-gain} = 0.168$ , indicating that an 80% depletion of eIF3k results in a 13.4% increase in the steady-state free ribosomal pool. This approximates the experimental findings that suggest between 10% and 15% increase in the steady-state free ribosomal pool at ~80% depletion of eIF3k.

#### Quantification and statistical analysis

All FDR and *P*-values for the RNA-seq data were calculated using EdgeR in R. Statistical analysis of the remaining datasets

(proteomic and TE) was performed with Microsoft Excel. *P*-values for the remaining datasets were determined using the multiple *t*-tests function (two-stage step-up method of Benjamini, Krieger, and Yekutieli) and unpaired Student's *t*-test in GraphPad Prism 8.

## Data availability

RNA-seq data were deposited into European Nucleotide Archive (accession number: PRJEB53197) and are available at <https://www.ebi.ac.uk/ena/browser/view/PRJEB53197>. Proteomic data were deposited to ProteomeXchange via PRIDE (accession number: PXD034084) and are available at <https://proteomecentral.proteomexchange.org/cgi/GetDataset?ID=PX034084>.

Expanded View for this article is available online.

## Acknowledgements

We thank R. Ding and the Mass Spectrometry Facility of the School of Pharmaceutical Sciences at Xiamen University for support. The support from the Equipment Platform of the State Key Lab of Cellular Stress Biology at Xiamen University is gratefully acknowledged. This work was funded through grants 81773771 and 31770813 from the National Science Foundation of China (DAW), the Natural Science Foundation of Fujian Province (2018J01053), the Fujian Province Science and Technology Pilot Project (2021Y0002), the Fundamental Research Funds for the Central Universities (20720220053), and the Innovation Program of Xiamen University Department of Life Sciences & Human Health (YC). RR is supported by the European Research Council (Consolidator Grant PACA-MET and MSCA-ITN-ETN PRECODE), the Deutsche Forschungsgemeinschaft (DFG RA1629/2-1; DFG RA1629/4-1; SFB1321; SFB1335), the German Cancer Consortium, and the Deutsche Krebshilfe (70114314). Additional funding was provided by the Zimin Institute for Engineering Solutions Advancing Better Lives (TT) and from hospital funds (XK). Open Access funding enabled and organized by Projekt DEAL.

## Author contributions

**Dieter A Wolf:** Conceptualization; data curation; formal analysis; supervision; funding acquisition; validation; visualization; writing – original draft; project administration; writing – review and editing. **Haoran Duan:** Conceptualization; data curation; formal analysis; validation; investigation; visualization; methodology; project administration; writing – review and editing. **Siqiong Zhang:** Formal analysis; investigation. **Yoram Zarai:** Conceptualization; formal analysis; investigation; visualization; methodology. **Rupert Öllinger:** Formal analysis; investigation. **Yanmeng Wu:** Formal analysis; investigation. **Li Sun:** Formal analysis; investigation. **Cheng Hu:** Formal analysis; investigation. **Yaohui He:** Formal analysis; methodology. **Guiyou Tian:** Formal analysis; investigation. **Roland Rad:** Supervision; funding acquisition. **Xiangquan Kong:** Resources; funding acquisition. **Tamir Tuller:** Conceptualization; formal analysis; supervision; funding acquisition; investigation; methodology; writing – review and editing. **Yabin Cheng:** Supervision; funding acquisition; writing – review and editing.

## Disclosure and competing interests statement

The authors declare that they have no conflict of interest.



## References

- Aguero T, Jin Z, Chorghade S, Kalsotra A, King ML, Yang J (2017) Maternal dead-end 1 promotes translation of nanos1 by binding the eIF3 complex. *Development* 144: 3755–3765
- Blažie SM, Takayanagi-Kiya S, McCulloch KM, Jin Y (2021) Eukaryotic initiation factor EIF-3.G augments mRNA translation efficiency to regulate neuronal activity. *Elife* 10: e68336
- Cattie DJ, Richardson CE, Reddy KC, Ness-Cohn EM, Droste R, Thompson MK, Gilbert WV, Kim DH (2016) Mutations in nonessential eIF3k and eIF3l genes confer lifespan extension and enhanced resistance to ER stress in *Caenorhabditis elegans*. *PLoS Genet* 12: e1006326
- Chandrashekar DS, Karthikeyan SK, Korla PK, Patel H, Shovon AR, Athar M, Netto GJ, Qin ZS, Kumar S, Manne U et al (2022) UALCAN: an update to the integrated cancer data analysis platform. *Neoplasia* 25: 18–27
- Chen J, Wei Y, Feng Q, Ren L, He G, Chang W, Zhu D, Yi T, Lin Q, Tang W et al (2016) Ribosomal protein S15A promotes malignant transformation and predicts poor outcome in colorectal cancer through misregulation of p53 signaling pathway. *Int J Oncol* 48: 1628–1638
- Chen F, Chandrashekar DS, Varambally S, Creighton CJ (2019) Pan-cancer molecular subtypes revealed by mass-spectrometry-based proteomic characterization of more than 500 human cancers. *Nat Commun* 10: 5679
- Concordet J-P, Haeussler M (2018) CRISPOR: intuitive guide selection for CRISPR/Cas9 genome editing experiments and screens. *Nucleic Acids Res* 46: W242–W245
- Cox J, Matic I, Hilger M, Nagaraj N, Selbach M, Olsen JV, Mann M (2009) A practical guide to the MaxQuant computational platform for SILAC-based quantitative proteomics. *Nat Protoc* 4: 698–705
- Dai X, Zhu M (2020) Coupling of ribosome synthesis and translational capacity with cell growth. *Trends Biochem Sci* 45: 681–692
- Dai P, Wang X, Gou L-T, Li Z-T, Wen Z, Chen Z-G, Hua M-M, Zhong A, Wang L, Su H et al (2019) A translation-activating function of MIWI/piRNA during mouse spermiogenesis. *Cell* 179: 1566–1581
- Dana A, Tuller T (2015) Mean of the typical decoding rates: a new translation efficiency index based on the analysis of ribosome profiling data. *G3 (Bethesda)* 5: 73–80
- Darnell JC, Van Driesche SJ, Zhang C, Hung KYS, Mele A, Fraser CE, Stone EF, Chen C, Fak JJ, Chi SW et al (2011) FMRP stalls ribosomal translocation on mRNAs linked to synaptic function and autism. *Cell* 146: 247–261
- De Silva D, Ferguson L, Chin GH, Smith BE, Apathy RA, Roth TL, Blaeschke F, Kudla M, Marson A, Ingolia NT et al (2021) Robust T cell activation requires an eIF3-driven burst in T cell receptor translation. *Elife* 10: e74272
- des Georges A, Dhote V, Kuhn L, Hellen CUT, Pestova TV, Frank J, Hashem Y (2015) Structure of mammalian eIF3 in the context of the 43S preinitiation complex. *Nature* 525: 491–495
- Docquier A, Pavlin L, Raibon A, Bertrand-Gaday C, Sar C, Leibovitch S, Candau R, Bernardi H (2019) eIF3f depletion impedes mouse embryonic development, reduces adult skeletal muscle mass and amplifies muscle loss during disuse. *J Physiol* 597: 3107–3131
- Eliseev B, Yeramala L, Leitner A, Karuppasamy M, Raimondeau E, Huard K, Alkalaeva E, Aebersold R, Schaffitzel C (2018) Structure of a human cap-dependent 48S translation pre-initiation complex. *Nucleic Acids Res* 46: 2678–2689
- Fujii K, Zhulyn O, Byeon GW, Genuth NR, Kerr CH, Walsh EM, Barna M (2021) Controlling tissue patterning by translational regulation of signaling transcripts through the core translation factor eIF3c. *Dev Cell* 56: 2928–2937
- Fusco CM, Desch K, Dörrbaum AR, Wang M, Staab A, Chan ICW, Vail E, Villier V, Langer JD, Schuman EM (2021) Neuronal ribosomes exhibit dynamic and context-dependent exchange of ribosomal proteins. *Nat Commun* 12: 6127
- Guo P, Wang Y, Dai C, Tao C, Wu F, Xie X, Yu H, Zhu Q, Li J, Ye L et al (2018) Ribosomal protein S15a promotes tumor angiogenesis via enhancing Wnt/ $\beta$ -catenin-induced FGF18 expression in hepatocellular carcinoma. *Oncogene* 37: 1220–1236
- Hashem Y, des Georges A, Dhote V, Langlois R, Liao HY, Grassucci RA, Hellen CUT, Pestova TV, Frank J (2013) Structure of the mammalian ribosomal 43S preinitiation complex bound to the scanning factor DHX29. *Cell* 153: 1108–1119
- Henley SA, Dick FA (2012) The retinoblastoma family of proteins and their regulatory functions in the mammalian cell division cycle. *Cell Div* 7: 10
- Herrmannová A, Prilepskaja T, Wagner S, Šikrová D, Zeman J, Poncová K, Valášek LS (2020) Adapted formaldehyde gradient cross-linking protocol implicates human eIF3d and eIF3c, k and l subunits in the 43S and 48S pre-initiation complex assembly, respectively. *Nucleic Acids Res* 48: 1969–1984
- Hershey JWB (2015) The role of eIF3 and its individual subunits in cancer. *Biochim Biophys Acta* 1849: 792–800
- Jin A, Itahana K, O'Keefe K, Zhang Y (2004) Inhibition of HDM2 and activation of p53 by ribosomal protein L23. *Mol Cell Biol* 24: 7669–7680
- Korem Kohanim Y, Levi D, Jona G, Towbin BD, Bren A, Alon U (2018) A bacterial growth law out of steady state. *Cell Rep* 23: 2891–2900
- Kumar P, Hellen CUT, Pestova TV (2016) Toward the mechanism of eIF4F-mediated ribosomal attachment to mammalian capped mRNAs. *Genes Dev* 30: 1573–1588
- Lamper AM, Fleming RH, Ladd KM, Lee ASY (2020) A phosphorylation-regulated eIF3d translation switch mediates cellular adaptation to metabolic stress. *Science* 370: 853–856
- Lee MV, Topper SE, Hubler SL, Hose J, Wenger CD, Coon JJ, Gasch AP (2011) A dynamic model of proteome changes reveals new roles for transcript alteration in yeast. *Mol Syst Biol* 7: 514
- Lee ASY, Kranzusch PJ, Cate JHD (2015) eIF3 targets cell-proliferation messenger RNAs for translational activation or repression. *Nature* 522: 111–114
- Lee ASY, Kranzusch PJ, Doudna JA, Cate JHD (2016) eIF3d is an mRNA cap-binding protein that is required for specialized translation initiation. *Nature* 536: 96–99
- Lin Y, Li F, Huang L, Polte C, Duan H, Fang J, Sun L, Xing X, Tian G, Cheng Y et al (2020) eIF3 associates with 80S ribosomes to promote translation elongation, mitochondrial homeostasis, and muscle health. *Mol Cell* 79: 575–587
- Liu C, He X, Liu X, Yu J, Zhang M, Yu F, Wang Y (2019) RPS15A promotes gastric cancer progression via activation of the Akt/IKK- $\beta$ /NF- $\kappa$ B signalling pathway. *J Cell Mol Med* 23: 2207–2218
- Lohrum MAE, Ludwig RL, Kubbutat MHC, Hanlon M, Vousden KH (2003) Regulation of HDM2 activity by the ribosomal protein L11. *Cancer Cell* 3: 577–587
- Luo J, Solimini NL, Elledge SJ (2009) Principles of cancer therapy: oncogene and non-oncogene addiction. *Cell* 136: 823–837
- Macosko EZ, Basu A, Satija R, Nemes J, Shekhar K, Goldman M, Tirosh I, Bialas AR, Kamitaki N, Martersteck EM et al (2015) Highly parallel genome-wide expression profiling of individual cells using nanoliter droplets. *Cell* 161: 1202–1214
- Marchione R, Leibovitch SA, Lenormand J-L (2013) The translational factor eIF3f: the ambivalent eIF3 subunit. *Cell Mol Life Sci* 70: 3603–3616
- Meyer KD, Patil DP, Zhou J, Zinoviev A, Skabkin MA, Elemento O, Pestova TV, Qian S-B, Jaffrey SR (2015) 5' UTR m6A promotes cap-independent translation. *Cell* 163: 999–1010

- Meyuhas O (2000) Synthesis of the translational apparatus is regulated at the translational level. *Eur J Biochem* 267: 6321–6330
- Mori M, Schink S, Erickson DW, Gerland U, Hwa T (2017) Quantifying the benefit of a proteome reserve in fluctuating environments. *Nat Commun* 8: 1225
- Natsume T, Kiyomitsu T, Saga Y, Kanemaki MT (2016) Rapid protein depletion in human cells by auxin-inducible degron tagging with short homology donors. *Cell Rep* 15: 210–218
- Parekh S, Ziegenhain C, Vieth B, Enard W, Hellmann I (2016) The impact of amplification on differential expression analyses by RNA-seq. *Sci Rep* 6: 25533
- Pulos-Holmes MC, Srole DN, Juarez MG, Lee AS-Y, McSwiggen DT, Ingolia NT, Cate JH (2019) Repression of ferritin light chain translation by human eIF3. *Elife* 8: e48193
- Ran FA, Hsu PD, Wright J, Agarwala V, Scott DA, Zhang F (2013) Genome engineering using the CRISPR-Cas9 system. *Nat Protoc* 8: 2281–2308
- Raveh A, Margaliot M, Sontag ED, Tuller T (2016) A model for competition for ribosomes in the cell. *J R Soc Interface* 13: 20151062
- Reuveni S, Meilijson I, Kupiec M, Ruppin E, Tuller T (2011) Genome-scale analysis of translation elongation with a ribosome flow model. *PLoS Comput Biol* 7: e1002127
- Robinson MD, McCarthy DJ, Smyth GK (2010) edgeR: a Bioconductor package for differential expression analysis of digital gene expression data. *Bioinformatics* 26: 139–140
- Sadato D, Ono T, Gotoh-Saito S, Kajiwara N, Nomura N, Ukaji M, Yang L, Sakimura K, Tajima Y, Oboki K et al (2018) Eukaryotic translation initiation factor 3 (eIF3) subunit e is essential for embryonic development and cell proliferation. *FEBS Open Bio* 8: 1188–1201
- Schneider CA, Rasband WS, Eliceiri KW (2012) NIH Image to ImageJ: 25 years of image analysis. *Nat Methods* 9: 671–675
- Selbach M, Schwanhäusser B, Thierfelder N, Fang Z, Khanin R, Rajewsky N (2008) Widespread changes in protein synthesis induced by microRNAs. *Nature* 455: 58–63
- Sesen J, Casas J, Scotland SJ, Seva C, Eisinger-Mathason TSK, Skuli N (2017) The bad, the good and eIF3e/INT6. *Front Biosci (Landmark Ed)* 22: 1–20
- Shah M, Su D, Scheliga JS, Pluskal T, Boronati S, Motamedchaboki K, Campos AR, Qi F, Hidalgo E, Yanagida M et al (2016) A transcript-specific eIF3 complex mediates global translational control of energy metabolism. *Cell Rep* 16: 1891–1902
- Shi J, Kahle A, Hershey JWB, Honchak BM, Warneke JA, Leong SPL, Nelson MA (2006) Decreased expression of eukaryotic initiation factor 3f deregulates translation and apoptosis in tumor cells. *Oncogene* 25: 4923–4936
- Simonetti A, Brito Querido J, Myasnikov AG, Mancera-Martinez E, Renaud A, Kuhn L, Hashem Y (2016) eIF3 peripheral subunits rearrangement after mRNA binding and start-codon recognition. *Mol Cell* 63: 206–217
- Slavov N, Semrau S, Airoidi E, Budnik B, van Oudenaarden A (2015) Differential stoichiometry among core ribosomal proteins. *Cell Rep* 13: 865–873
- Smith MD, Arake-Tacca L, Nitido A, Montabana E, Park A, Cate JH (2016) Assembly of eIF3 mediated by mutually dependent subunit insertion. *Structure* 24: 886–896
- Sonenberg N, Hinnebusch AG (2009) Regulation of translation initiation in eukaryotes: mechanisms and biological targets. *Cell* 136: 731–745
- Thoms M, Buschauer R, Ameismeier M, Koepke L, Denk T, Hirschenberger M, Kratzat H, Hayn M, Mackens-Kiani T, Cheng J et al (2020) Structural basis for translational shutdown and immune evasion by the Nsp1 protein of SARS-CoV-2. *Science* 369: 1249–1255
- Tian G, Hu C, Yun Y, Yang W, Dubiel W, Cheng Y, Wolf DA (2021) Dual roles of HSP70 chaperone HSPA1 in quality control of nascent and newly synthesized proteins. *EMBO J* 40: e106183
- Tuller T, Zur H (2015) Multiple roles of the coding sequence 5' end in gene expression regulation. *Nucleic Acids Res* 43: 13–28
- Valášek LS, Zeman J, Wagner S, Beznosková P, Pavlíková Z, Mohammad MP, Hronová V, Herrmannová A, Hashem Y, Gunišová S (2017) Embraced by eIF3: structural and functional insights into the roles of eIF3 across the translation cycle. *Nucleic Acids Res* 45: 10948–10968
- Wagner S, Herrmannová A, Malík R, Peclínová L, Valášek LS (2014) Functional and biochemical characterization of human eukaryotic translation initiation factor 3 in living cells. *Mol Cell Biol* 34: 3041–3052
- Wagner S, Herrmannová A, Šíková D, Valášek LS (2016) Human eIF3b and eIF3a serve as the nucleation core for the assembly of eIF3 into two interconnected modules: the yeast-like core and the octamer. *Nucleic Acids Res* 44: 10772–10788
- Wićniewski JR, Ostasiewicz P, Mann M (2011) High recovery FASP applied to the proteomic analysis of microdissected formalin fixed paraffin embedded cancer tissues retrieves known colon cancer markers. *J Proteome Res* 10: 3040–3049
- Wolf DA, Lin Y, Duan H, Cheng Y (2020) eIF-three to tango: emerging functions of translation initiation factor eIF3 in protein synthesis and disease. *J Mol Cell Biol* 12: 403–409
- Wool IG (1996) Extraribosomal functions of ribosomal proteins. *Trends Biochem Sci* 21: 164–165
- Wu X, Shi T, He Y, Wang F, Sang R, Ding J, Zhang W, Shu X, Shen H, Yi J et al (2017) Methylation of transcription factor YY2 regulates its transcriptional activity and cell proliferation. *Cell Discov* 3: 17035
- Yan X, Hoek TA, Vale RD, Tanenbaum ME (2016) Dynamics of translation of single mRNA molecules In vivo. *Cell* 165: 976–989
- Yen H-CS, Chang EC (2000) Yin6, a fission yeast Int6 homolog, complexes with Moe1 and plays a role in chromosome segregation. *Proc Natl Acad Sci U S A* 97: 14370–14375
- Yu R, Campbell K, Pereira R, Björkeröth J, Qi Q, Vorontsov E, Sihlbom C, Nielsen J (2020) Nitrogen limitation reveals large reserves in metabolic and translational capacities of yeast. *Nat Commun* 11: 1881
- Zarai Y, Tuller T (2018) Computational analysis of the oscillatory behavior at the translation level induced by mRNA levels oscillations due to finite intracellular resources. *PLoS Comput Biol* 14: e1006055
- Zhang Y, Wolf GW, Bhat K, Jin A, Allio T, Burkhart WA, Xiong Y (2003) Ribosomal protein L11 negatively regulates oncoprotein MDM2 and mediates a p53-dependent ribosomal-stress checkpoint pathway. *Mol Cell Biol* 23: 8902–8912
- Zhou C, Arslan F, Wee S, Krishnan S, Ivanov AR, Oliva A, Leatherwood J, Wolf DA (2005) PCI proteins eIF3e and eIF3m define distinct translation initiation factor 3 complexes. *BMC Biol* 3: 14
- Zhou M, Sandercock AM, Fraser CS, Ridlova G, Stephens E, Schenauer MR, Yokoi-Fong T, Barsky D, Leary JA, Hershey JW et al (2008) Mass spectrometry reveals modularity and a complete subunit interaction map of the eukaryotic translation factor eIF3. *Proc Natl Acad Sci U S A* 105: 18139–18144
- Zhou Y, Zhou B, Pache L, Chang M, Khodabakhshi AH, Tanaseichuk O, Benner C, Chanda SK (2019) Metascape provides a biologist-oriented resource for the analysis of systems-level datasets. *Nat Commun* 10: 1523



**License:** This is an open access article under the terms of the [Creative Commons Attribution-NonCommercial-NoDerivs](https://creativecommons.org/licenses/by-nc-nd/4.0/) License, which permits use and distribution in any medium, provided the original work is properly cited, the use is non-commercial and no modifications or adaptations are made.